MECHANICAL ENGINEERING SCIENCE

ISSN:2661-4448(online)
2661-443X(print)
Volume 7 No.1 2025

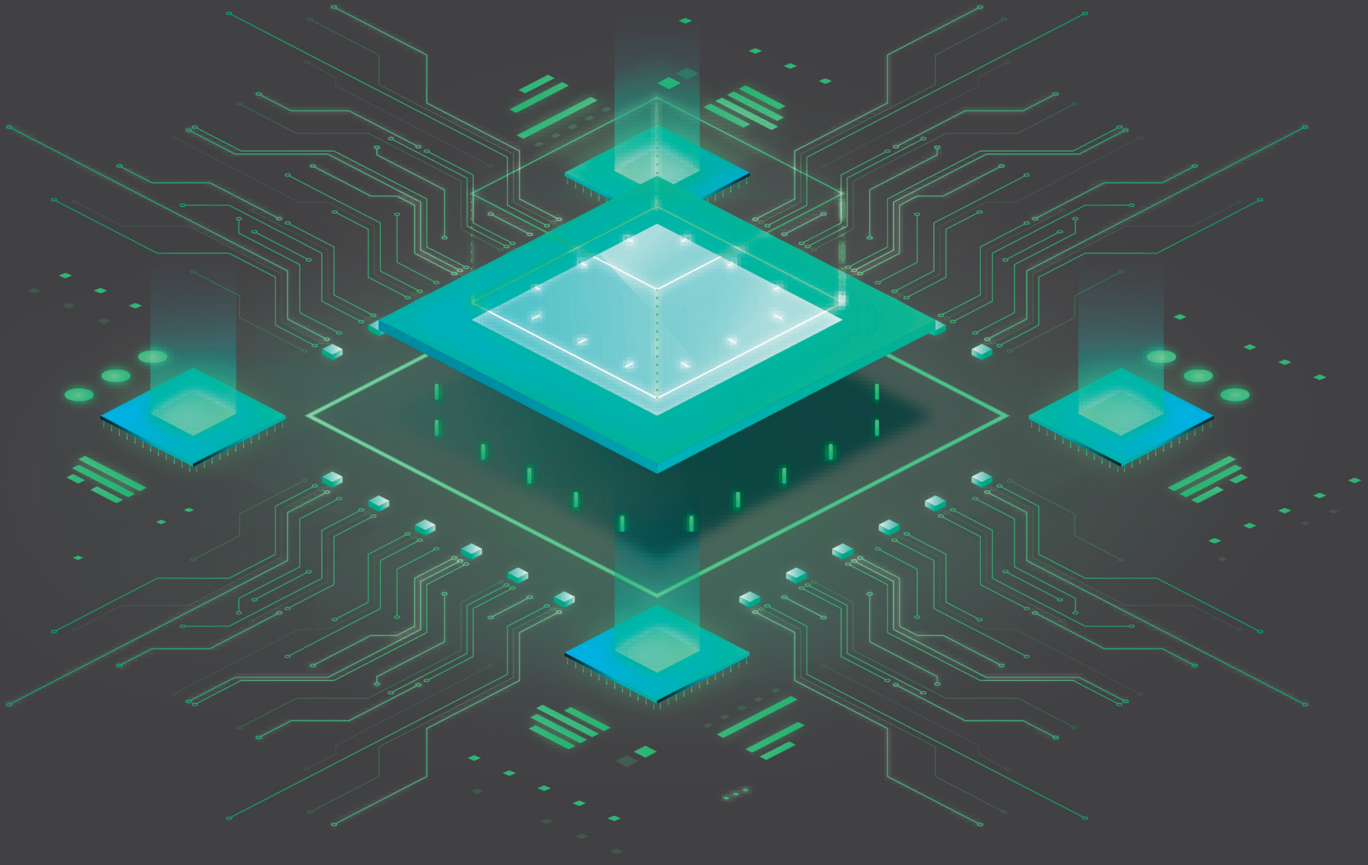

VISER
www.viserdata.com

COMPANY INTRODUCTION

Viser Technology Pte. Ltd. was founded in Singapore with branch offices in both Hebei and Chongqing, China. Viser focuses on publishing scientific and technological journals and books that promote the exchange of scientific and technological findings among the research community and around the globe. Despite being a young company, Viser is actively connecting with well-known universities, research institutes, and indexation database, and has already established a stable collaborative relationship with them. We also have a group of experienced editors and publishing experts who are dedicated to publishing high-quality journal and book contents. We offer the scholars various academic journals covering a variety of subjects and we are committed to reducing the hassles of scholarly publishing. To achieve this goal, we provide scholars with an all-in-one platform that offers solutions to every publishing process that a scholar needs to go through in order to show their latest finding to the world.

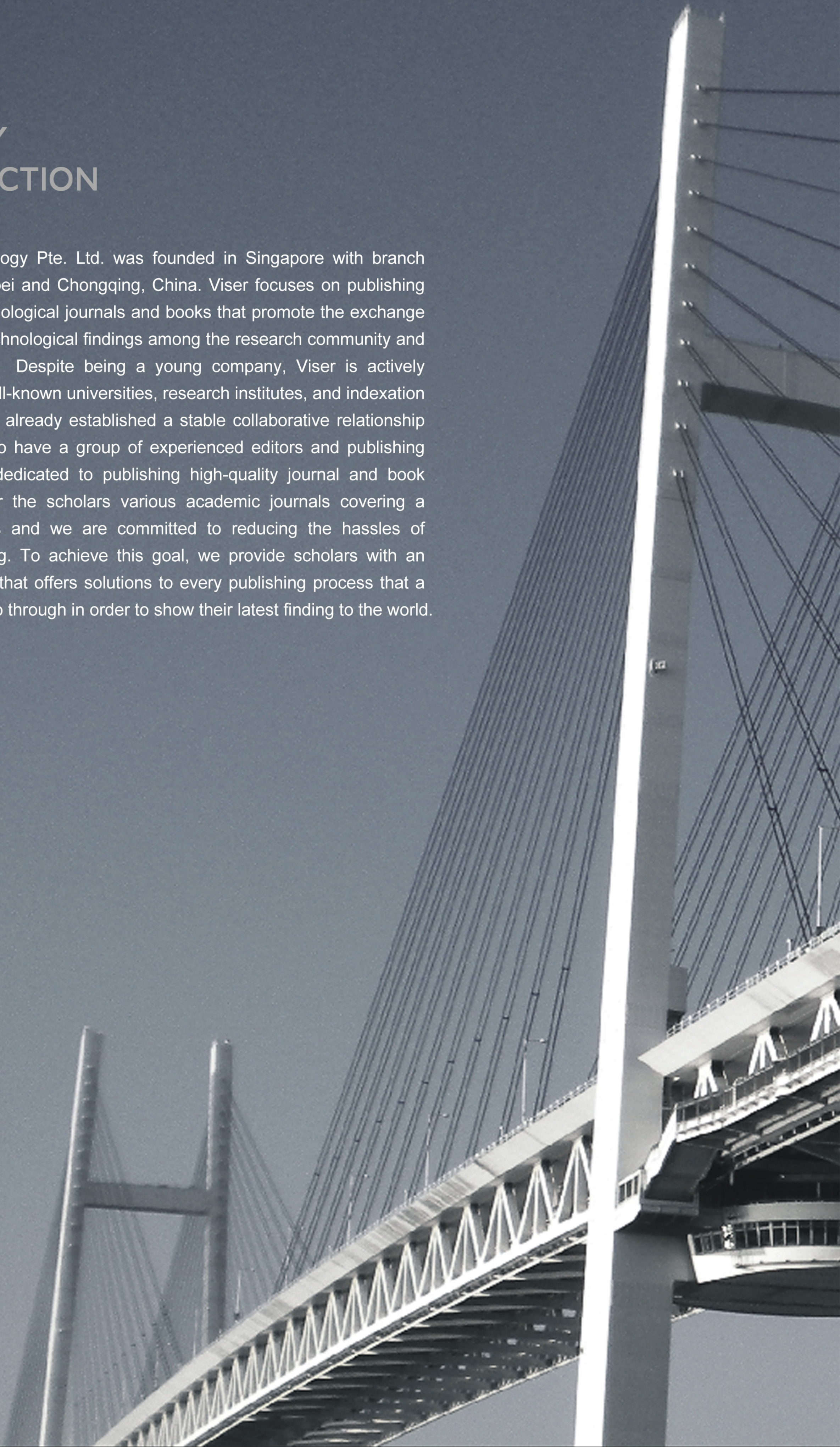

Mechanical Engineering Science

Publisher: Viser Technology Pte. Ltd.
ISSN: 2661-4448(online)
2661-443X(print)
Frequency: Semi-annual
Add.: 111 North Bridge Rd, #21-01 Peninsula Plaza,
Singapore 179098
https://www.viserdata.com/

Editors:
Yajun LIAN
John WILSON
Mart CHEN
Debra HAMILTON
Jennifer M DOHY
Edward Adam Davis
Yanli LIU
Nike Yough
Qiuyue SU
Xin DI
Xiuli LI
Designer: Anson CHEE

Mechanical Engineering Science

Volume 7 No.1 (2025)

CONTENTS

VISER

Viser Technology Pte. Ltd.
Mechanical Engineering Science
DOI: 10.33142/mes.v7i1.16747

Research Article **Open Access**

Design of Automatic Correction Device for Belt Conveyor

Pengxiang ZHAO[1], Wenwu ZHANG[1*], Guangchen XU[1], Yu XU[1], Zhengliang ZHANG[1], Xueshu LIU[2]

1. Yingkou Institute of Technology, Yingkou, Liaoning, 115017, China
2. Yingkou Hengsheng Machinery Processing Co., Ltd., Yingkou, Liaoning, 115000, China

[*]***Corresponding Author:*** *Wenwu ZHANG, E-mail: address:zhangwenwu@yku.edu.cn*

Abstract

Belt conveyors are prone to problems such as conveyor belt deviation during operation. The main correction method is to adjust the angle of the roller frame, but the current adjustment is mostly manual. In order to solve the problem of low equipment transportation efficiency and low safety caused by conveyor belt deviation, a detection mechanism that can effectively detect conveyor belt deviation parameters is designed, and the working condition information is accurately transmitted to the PLC controller. If an abnormality is found, the designed correction device will correct the deviation, effectively ensuring the reliable and stable operation of the belt conveyor.

Keywords: *belt conveyor; deviation correction; fully automatic*

1 Introduction

Belt conveyors have the advantages of long conveying distance, low manual intervention, reliable performance, easy maintenance, high efficiency and energy saving. They are widely used in chemical, mining, agriculture and other industries, saving a lot of costs for the transportation of large and small pieces. They play an important role in industrial assembly line operations, and their operation directly affects the stability of the entire production process. Among the failures that occur during the operation of belt conveyors, conveyor belt deviation is a major problem. "Deviation" is due to the unique dynamic characteristics and structure of belt conveyors. During the operation, the conveyor belt deviates from the established center line track due to uneven force.

Many scholars have conducted in-depth research on this issue. Wang Yemu [1] analyzed the causes of conveyor belt deviation and designed an automatic feeding and correction control system based on hydraulic power source and PLC control system for coal mine conveyor belts. The experimental results show that the automatic correction control system uses hydraulic devices to respond quickly to deviations and can correct the production affected by conveyor belt deviation in a short time. Yu Ruixiang [2] designed an automatic correction device based on machine vision technology. Through image preprocessing, feature extraction and other steps, it automatically identifies and extracts the angle deviation of image fault-deviation, records the fault image in real time and performs timely correction processing. It has greatly improved the correction accuracy and work efficiency.Zhao Puhui [3] proposed an active deviation correction scheme that integrates deviation detection, automatic deviation correction, and intelligent protection. The system uses a deviation correction vertical roller with a two-stage rotating mechanism as the core mechanism for deviation detection and correction, and designs a corresponding monitoring system. The experimental results show that the design realizes active belt deviation correction without human intervention. The traditional deviation correction process requires stopping the machine to correct the conveyor belt, which will affect the production progress and increase unnecessary working time [4]. Therefore, in response to the above problems, this paper designs a fully automatic deviation correction system for belt conveyors. The deviation correction is carried out by adjusting the swing angle of the roller frame, and the roller frame is controlled by a control system to achieve the purpose of fully automatic deviation correction. It can effectively reduce a series of indirect hazards such as resource waste, environmental pollution, and fire safety, and reduce the dependence of belt conveyor deviation correction on human resources, thereby forming a virtuous cycle in all aspects.

2 Structure Design Cheme of Automatic Correction Device

2.1 The overall structure of automatic correction device

The belt conveyor automatic deviation correction

Received on March 8th, 2025; Accepted on April 13, 2025

device consists of induction rollers, bearings and rotating shafts, bearing seats, support rollers, conveyor belts, detection roller fixing brackets, angle sensors, shaft rotation angle encoders, conveyor roller frames, etc., as shown in Figure 1.

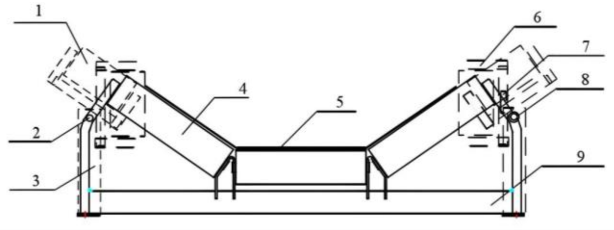

1-induction roller;2-bearings and rotating shafts;3-bearing seats;4-support rollers;5-conveyor belts; 6-detection roller fixing brackets;7-angle sensors;8-shaft rotation angle encoders 9-conveyor roller frames

Figure 1 Overall structure diagram of the fully automatic deviation correction system

2.2 Working principle of automatic deviation correction device

When the device is in use, the angle encoder 7 is connected to the rotating shaft 2 of the roller frame. When the conveyor belt 5 deviates, it will push the roller frame 1, thereby triggering the angle encoder 7. The angle encoder 8 transmits the signal to the controller, and the controller calculates the deviation amount according to the preset algorithm. The edge of the conveyor belt 5 is pushed to make the inclination sensor and the roller frame 1 swing. The inclination sensor transmits the inclination change signal to the controller, and the controller calculates the deviation angle accordingly; when the angle is detected to be offset, the push rod motor is started, and the push motor frame starts to move in the track. There is a correction roller and the auxiliary plate end hinged. When the push motor is in action, it calculates the offset distance according to the controller and automatically adjusts the position of the correction roller, so that the material is sorted.

3 Automatic Correction Device Main System Design

The automatic correction device consists of three systems: detection system, correction system and control system.

3.1 Design of automatic correction device detection system

The detection system is used to detect the running position and running trend of the conveyor belt. The angle encoder is connected to the rotating shaft of the roller frame. When the conveyor belt deviates, it pushes the roller frame, thereby triggering the angle encoder [5]. The angle encoder transmits the signal to the controller, and the controller calculates the deviation amount according to the preset algorithm. The edge of the conveyor belt is pushed, causing the inclination sensor and the roller frame to swing. The inclination sensor transmits the inclination change signal to the controller, and the controller calculates the deviation angle based on it [6].

There are four ways to install the detection device. They are front detection, return detection, single-side detection and double-side detection, as shown in Figure 2. When installed on one side, the induction roller should be moved to the center line of the conveyor belt, and the offset of one side is used to determine the position of the conveyor belt; when installed on both sides, the signals of the two roller frames are detected by each other, and the conveyor belt position information obtained is more accurate.

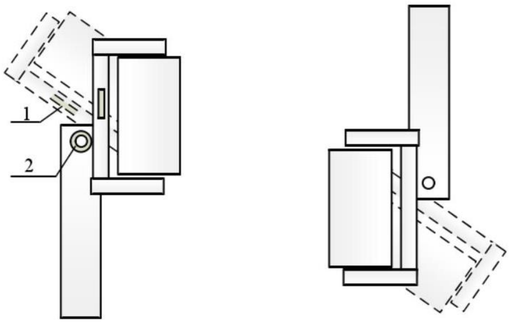

(a) Front deviation detection (b) Return deviation detection

1- Angle sensor; 2- Angle encoder

Figure 2 Detection system installation diagram

3.2 Design of automatic correction device correction system

The deviation correction system designed in this paper corrects the deviation by adjusting the angle between the return roller and the running direction of the conveyor belt. When the conveyor belt deviates, the angle between the return roller and the running direction of the conveyor belt is adjusted so that the return roller generates a traction force to the conveyor belt [7]. The force analysis is shown in Figure 3. α is the change in the angle of the return roller, F is the friction force exerted by the conveyor belt on the return roller, F_1 is the component force in the direction of rotation of the return roller, and F_2 is the component force in the direction of running of the conveyor belt. F_1 pulls the roller to rotate, and the F_2 roller generates a reverse friction force f on the conveyor belt. F_4 is the component force perpendicular to the running direction of the conveyor belt, thereby achieving the purpose of deviation correction.

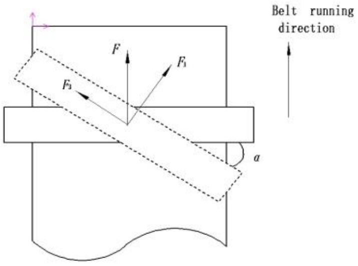

(a) Traction force F of conveyor belt on return roller

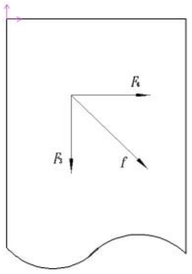

(b) Friction resistance f of roller on conveyor belt

Figure 3 Force analysis of roller angle change and correction

3.3 Design of control system for fully automatic deviation correction device

The control flow of the fully automatic deviation correction system is shown in Figure 4. The control system makes advance adjustments by predicting whether the conveyor belt has a tendency to deviate, and performs delayed deviation correction by detecting the current conveyor belt position. In this way, the conveyor belt running position can be controlled at the lowest cost. The prediction of the conveyor belt running trend is to analyze the recent trajectory of the conveyor belt, determine the conveyor belt deviation time, and issue adjustment commands to the drive device.

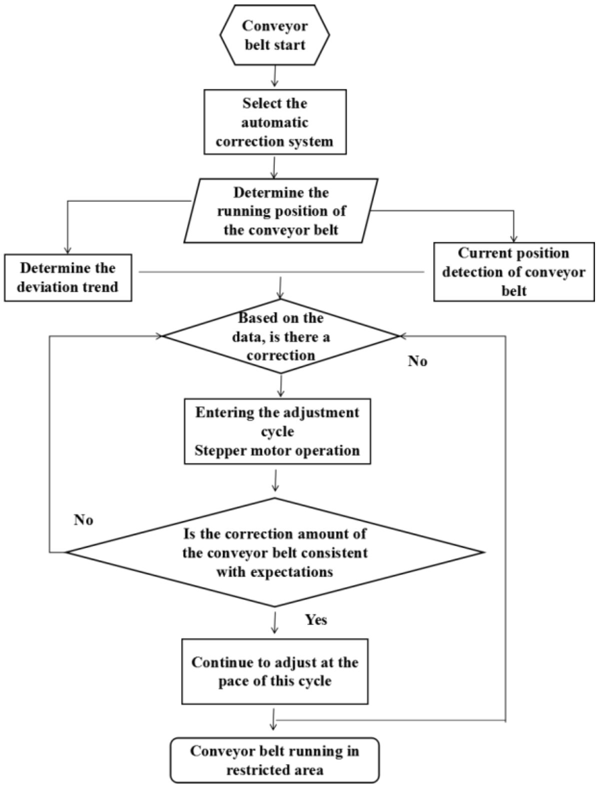

Figure 4 Control flow chart of the fully automatic deviation correction system

4 Conclusion

This paper designs a fully automatic deviation correction system for belt conveyors. This system does not require human intervention and will greatly reduce production costs.

(1) Find out the reasons for the deviation of the conveyor belt when carrying different materials under different stress conditions; formulate dynamic conveyor belt deviation correction measures, and come up with a solution for using rollers for deviation correction.

(2) Design a deviation detection device. Calculate the deviation of the conveyor belt by detecting the movement amplitude of the roller frame, and analyze the calculation method of the relationship between the movement amplitude of the roller frame and the deviation.

(3) Use automatic control logic to design a fully automatic deviation correction control system for belt conveyors, and predict and control the deviation in real time.

Fund Projects: The authors acknowledge the 2024 Yingkou Institute of Technology Undergraduate Innovation and Entrepreneurship Training Program; Yingkou Institute of Technology school-level scientific research project (Grant: ZDIL202302).

References

[1]Wang Ye-mu, Wang Yun-feng,Liu Cheng-bo,etc.Automatic Feeding and Correction Control System Based on PLC [J]. Coal Mine Machinery, 2017,38(2):178-179.

[2]Yu Rui-xiang,Ma Wei-jin,Huang Bin-cheng.Automatic Correction of Belt Conveyor Based on Machine Vision [J]. Coal Mine Machinery, 2013,34(7):162-164.

[3]Zhao Hui-pu.Design and application of intelligent dynamic deviation correction system for belt conveyor [J]. Mechanical Research & Application, 2024,37(2):155-157.

[4]Fan Bing-yao,Liu Guo-peng.Research on Application of Belt Conveyor Deviation Correction Control System [J]. Coal Mine Machinery, 2024,45(2):129-131.

[5]Wang Li-jun.Application of Hydraulic Control Deviation Correction Device for Mine Belt Conveyor [J]. Jiangxi Coal Science & Technology, 2023,(4):213-215,218.

[6]Zheng Yi.Research on Key Technologies of Automatic Deviation Correction System for Mining Belt Conveyor [J]. Mechanical Engineering & Automation, 2023,(4):191-192,194.

[7]Hou Jun-bo.Study on the influence of positive pressure of belt conveyor self-aligning roller on deviation correction ability [J]. Mechanical Management and Development, 2023,38(2):32-34,37.

Viser Technology Pte. Ltd.
Mechanical Engineering Science
DOI: 10.33142/mes.v7i1.16748

Research Article Open Access

Design of Campus Self-service Express Packaging Recycling Machine

Yu XU[1], Wenwu ZHANG[1*], Guangchen XU[1], Pengxiang ZHAO[1], Zhengliang ZHANG[1], Xueshu LIU[2]

1. Yingkou Institute of Technology, Yingkou, Liaoning, 115017, China

2. Yingkou Hengsheng Machinery Processing Co., Ltd., Yingkou, Liaoning, 115000, China

*****Corresponding Author:*** *Wenwu ZHANG, E-mail: address:zhangwenwu@yku.edu.cn*

Abstract

Based on the concept of sustainable design, we are committed to seeking innovative solutions and designing a complete express packaging recycling machine. The device consists of a vibration device, a compression device, a winding device and an electronic control system to promote the recycling of resources and environmental protection. This device can further improve the recycling efficiency and feasibility. It provides new ideas and solutions for the express industry and promotes the development of sustainable design in the field of express packaging recycling and reuse devices.

Keywords: *carton packaging; recycling machine design; strapping device; automatic recycling*

1 Introduction

With the rapid development of China's e-commerce platforms, online shopping has become a new trend, driving China to rank first in the world in the express delivery industry for ten consecutive years. In 2023, China's express delivery volume reached an astonishing 132 billion pieces, and the materials generated for packaging express delivery were extremely large. Among the express packaging materials, at least 44% of the materials can be recycled [1]. According to statistics, my country generates more than 9 million tons of paper waste each year, and my country's express packaging consumes about 32.8 billion cartons annually, which contains huge economic value. There are the following problems in the recycling of express packaging in my country:

(1) Lack of awareness of recycling express packaging. After unpacking the express delivery, most people take the goods away and then throw the express packaging away. They have a weak awareness of recycling, do not fully understand the added value of packaging, and cannot distinguish the properties of packaging materials. As a result, the materials that could have been recycled are mixed with various garbage because they cannot be sorted and recycled.

(2). There are problems with express packaging materials, such as non-environmental protection and excessive packaging. In order to reduce the cost of packaging materials, some companies use highly polluting materials to produce and package goods, without considering the impact on the environment and whether they can be recycled. At the same time, some companies over-package their products to make their products look beautiful and high-end, which not only increases the cost, but also many of the packaging materials used are not environmentally friendly materials, causing a great impact on the environment [2-4].

This paper designs a machine that can recycle express packaging cartons, which can not only improve the recycling efficiency of waste cartons, but also reduce the impact on the environment, which is in line with the social concept of green environmental protection.

2 The Overall Design Scheme of Express Packaging Recycling Machine

2.1 Overall structure of the express packaging recycling machine

The express packaging recycling machine is mainly composed of a vibration device, a compression device, a winding device and an electronic control system, as shown in Figure 1. The compression device includes a clamping mechanism and a hydraulic system. Since the winding device does not require too much power, but has certain requirements for accuracy, a servo motor is selected as the power source. The normal operation of the compression device and the winding device is

Received on March 11, 2025; Accepted on April 4th, 2025

precisely controlled by the PLC program set by the electronic control system, so that the two devices can coordinately complete the compression process of compressing the express packaging into the designed shape and the packaging process of wrapping the winding rope around the surface of the express packaging.

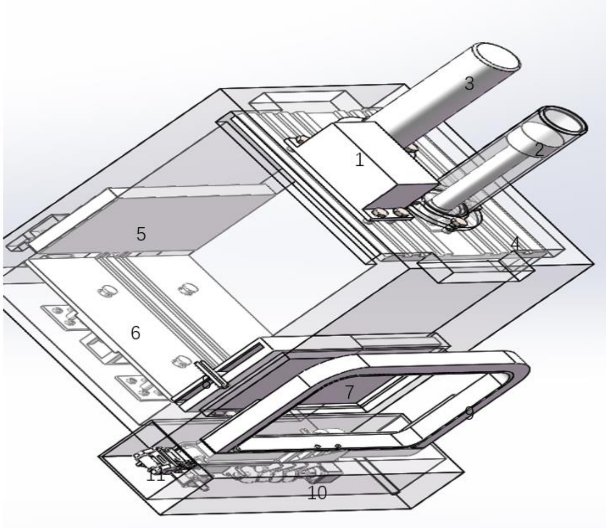

1 - Fuel tank; 2 - Piston rod; 3 - Hydraulic cylinder; 4 - Pressure plate; 5 - Push plate; 6 - Vibration plate; 7 - Front baffle; 8 - Hand push rod; 9 - Rope baffle; 10 - Coupling ;11 - Rope sheave

Figure 1 Structure diagram of express packaging recycling machine

2.2 Working Principle of Express Packaging Recycling Machine

When the weight of the package in the compression device of the express packaging recycling machine reaches the set value, the pressure sensor is triggered, and the auxiliary pressure block of the vibration mechanism compresses the package forward, and stops after reaching the designed position [5]. At this time, the hydraulic system starts to work, pressurizing and maintaining the pressure to the predetermined value. The front block of the winding device moves, and the rear pressure block pushes the paper ball forward through multiple pauses (the number of pauses is determined by the number set before compression). Each pause realizes the winding of the compressed paper ball once, so that the entire express packaging compression and winding process is completed and enters the next working cycle [6].

3 The Hydraulic System Design of Express Packaging Recycling Mmachine

3.1 The working requirements of hydraulic system

The requirements for the hydraulic system of the self-service express packaging recycling machine are relatively low. It only needs to achieve rapid descent to a certain height and then slowly pressurize the paper box until it reaches a certain height and then maintains pressure for a period of time to help the auxiliary push rod push the compressed paper box. After the bundling mechanism completes the bundling of the compressed paper box, it quickly returns to its original position and the entire working cycle is completed. There are no high requirements for accuracy and speed. The proposed hydraulic system circuit is shown in Figure 2.

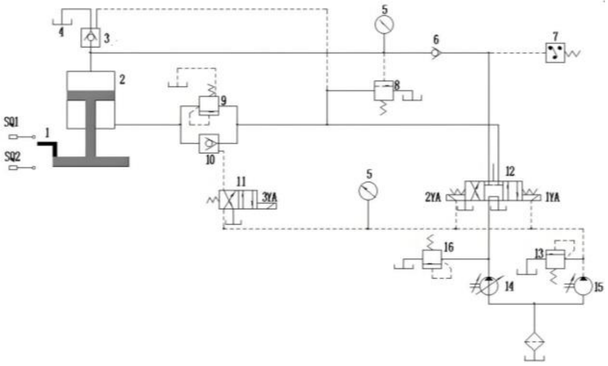

1-moving block; 2-hydraulic cylinder; 3,10-hydraulic control check valve; 4-oil tank; 5-pressure meter; 6-check valve; 7-pressure relay; 8-damped unloading valve; 9-back pressure valve; 11-two-position four-way electromagnetic directional valve; 12-three-position four-way electromagnetic directional valve; 13,16-overflow valve; 14,15-hydraulic pump SQ-stroke switch

Figure 2 Hydraulic system circuit diagram

3.2 Working process of hydraulic system

3.2.1 Hydraulic cylinder descends slowly

When the pressure detector of the compression mechanism detects that the pressure reaches the set value, the electromagnets IYA and 3YA are energized. The control oil output by the hydraulic pump 15 switches the three-position four-way electromagnetic reversing valve 12 to the right position on the one hand, and on the other hand, the hydraulic control check valve 10 opens when the electromagnetic reversing valve 11 is in the right position. At this time, the hydraulic cylinder and the moving block drop rapidly under the action of their own gravity. At this time, their gravity is greater than the resistance of the paper box to the block, and the hydraulic oil output by the hydraulic pump 14 is not enough to replenish the volume vacated in the upper chamber of the hydraulic cylinder. A partial vacuum is formed in the upper chamber of the hydraulic cylinder. The oil in the oil tank 4 located on the top of the hydraulic press enters the upper chamber of the hydraulic cylinder through the hydraulic control check valve 3 under the action of the atmosphere and the liquid level.

3.2.2 The hydraulic cylinder slowly approaches the carton and pressurizes it

When the moving block 1 on the slide hits the travel switch 2SQ, the electromagnet 3YA is de-energized, causing the reversing valve 11 to return to the left position and the hydraulically controlled one-way valve 10 to close. The oil in the lower part of the hydraulic cylinder must flow out through the back pressure valve 9, and the slide cannot descend by its own weight alone. The pressure in the upper chamber of the hydraulic cylinder 2 increases, the filling valve 3 closes, and the hydraulic cylinder 2 slowly approaches the compressed paper box. As the hydraulic cylinder 2 continues to descend, the load begins to increase continuously, causing the pressure in the upper chamber to further increase, and the output flow of the variable pump automatically decreases.

3.2.3 Hydraulic cylinder pressure maintenance

As the hydraulic piston moves downward, the pressure in the upper chamber of the hydraulic cylinder increases continuously. When the pressure in the upper part of the hydraulic cylinder reaches the set value, the pressure relay 7 will send a signal to the control system, causing the electromagnet 1YA to be powered off and the electromagnetic reversing valve 12 to move to the middle position. The purpose is to close the upper and lower oil chambers of the hydraulic cylinder, and the system starts to maintain pressure and maintain the current position. The function of the one-way valve 6 is mainly to ensure that the upper chamber of the hydraulic cylinder has good sealing properties, and at the same time, the upper chamber of the main cylinder can always maintain high pressure. The length of the pressure holding time can be adjusted by the time relay controlled by the pressure relay 7. The hydraulic pump 14 is unloaded through the middle position of the reversing valve 12.

3.2.4 Hydraulic cylinder depressurizes and returns

When the pressure holding time reaches the designed time, the time relay controlled by the pressure relay 7 sends a signal to notify the control system of the machine. After processing the transmitted signal, the control system of the machine energizes the electromagnet 2YA. At this time, the reversing valve 12 will switch to the left position, and the hydraulic cylinder is in the return state. During the pressure holding stage, the energy accumulated in the hydraulic cylinder is suddenly released to produce hydraulic shock, which will cause the equipment to vibrate and the pipeline to shake violently and emit huge noise. Therefore, after the pressure is held, the pressure is released first and then the return is made.

3.2.5 Stop

When the moving block 1 on the slide presses the travel switch 1SQ, the electromagnet 2YA is de-energized, the hydraulic cylinder stops moving, and the return stroke ends. At this time, the oil of the hydraulic pump 14 returns to the oil tank through the middle position of the reversing valve 12 and is in an unloaded state, and the entire working cycle is completed. The electromagnet action sequence of the hydraulic system is shown in Table 1.

Table 1 Electromagnet action sequence table of hydraulic system

Working condition	Signal source	Electromagnet 1YA	Electromagnet 2YA	Electromagnet 3YA
Fast down	Pressure detector	+	-	+
Slow pressure	Block press down travel switch SQ2	+	-	-
Holding pressure	Pressure relay	-	-	-
Releasing pressure return	Time relay	-	+	-
Stop	Block press down travel switch SQ1	-	-	-

4 Design of the Bundling Mechanism of the Express Packaging Recycling Machine

4.1 Design of strapping mechanism

The push block at the rear of the machine pushes the compressed paper ball forward with frequency, and the strapping mechanism straps the compressed paper ball. After multiple strappings are completed, the strapping mechanism stops working, the baffle at the rear of the machine automatically returns, and the hydraulic press mechanism also returns to its original position, and the entire working cycle is completed. The strapping mechanism structure is shown in Figure 3.

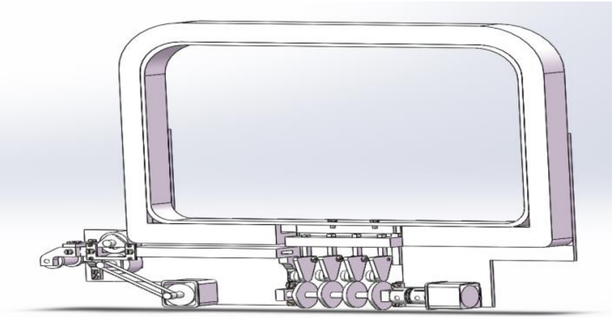

Figure 3 Structure diagram of bundling mechanism

The strapping mechanism is mainly composed of four cams of different shapes, a coupling, three motors, and strapping ropes. The working process is as follows: the package to be strapped is moved to the designated position, and the strapping rope moves forward under the push of the rubber wheel, and is pre-wound into the shape of a compressed package above the No. 1 cam. At this time, the pressure block above the cam presses the rope, and the No. 2 motor starts to work, causing the rope to fall downward under the action of its own gravity. At the same time, the No. 1 motor starts to reverse and tighten the rope. The size of the tension is set according to the actual situation of the paper ball. The block controlled by the No. 3 cam presses the rope, the block controlled by the No. 2 cam melts the rope, and the blade controlled by the No. 4 cam cuts off the excess rope to complete the complete strapping of the express package.

4.2 Cam mechanism design of strapping mechanism

Since the cam has fast response, high efficiency, simple structure and is not prone to failure, the cam is used to control the two fixation, melting and shearing of the binding rope.

4.2.1. Selection of cam and push rod

Since this mechanism requires four cams to move regularly on one axis, and the internal space of the strapping mechanism is limited, a disc cam is used[7].

Since this mechanism has high requirements for the precision of the push rod driven by the cam, the roller push rod has relatively small wear due to rolling friction between the roller and the cam profile, and the precision meets the requirements of this mechanism, so the roller push rod is selected. Finally, a disc cam mechanism is selected.

4.2.2. Design of cam profile

As shown in Figure 4, establish an OXY coordinate system, where the origin is the center of the cam base circle, and *B₀* is the starting point of the cam push stroke contour line. At the beginning, the center of the push rod roller is located at *B₀*. When the cam rotates through an angle of δ, the push rod produces a corresponding displacement *s*. The center of the roller is located at point *B*, and its rectangular coordinate B ($x=\left(s_0+s\right)\sin\delta$, $y=\left(s_0+s\right)\cos\delta$) is the theoretical contour curve of the cam. Since the distance between the working curve and the theoretical curve in the normal direction is equal to the roller radius *R*, when determining a point $B(x,y)$ on the theoretical curve, it is only necessary to take a distance *R* along the normal direction of the theoretical curve at this point to obtain the corresponding point $B'(x',y')$ of the curve, where:

$$\sin\theta=\left(\mathrm{d}x/\,d\delta\right)/\sqrt{\left(\mathrm{d}x/\,d\delta\right)^2+\left(\mathrm{d}y/\,d\delta\right)^2}$$

$$\cos\theta=-\left(\mathrm{d}y/\,d\delta\right)/\sqrt{\left(\mathrm{d}x/\,d\delta\right)^2+\left(\mathrm{d}y/\,d\delta\right)^2} \tag{1}$$

Its coordinate $B'(x'=x\mp r_r\cos\theta, y'=y\mp r_r sin\theta)$ is the working contour equation of the cam.

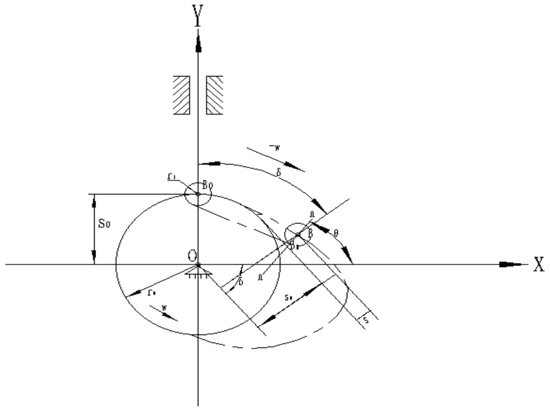

Figure 4 Cam contour line diagram

5 Conclusion

(1) Design a set of low-cost, safe and efficient recycling principle solutions suitable for express packaging in multiple scenarios.

(2) According to the planned solution, establish basic physical models and mathematical models, conduct simple kinematic analysis on the compression mechanism and strapping mechanism of the recycling machine, judge whether the design is reasonable, and provide a theoretical basis for the subsequent design of various parts of the recycling machine.

(3) Reasonably select and coordinate the required motors, hydraulic system cams and other mechanisms, while completing basic tasks without increasing additional costs, and improve economic benefits.

Fund Projects: The authors acknowledge the 2024 Yingkou Institute of Technology Undergraduate Innovation and Entrepreneurship Training Program; Yingkou Institute of Technology school level scientific research project (Grant: ZDIL202302).

References

[1] Nuzat Nuary Alam, Md Mehrab Sadik. Development of a recycling machine for co-nstructing synthetic yarn from plastic waste[J]. MethodsX, 2024,121-131.

[2] Shi Fei.Industrial green transformation: a duet of policy drive and innovative practice [J]. China Information Technology, 2024,(5):21-22.

[3] Zhao Di,Xing Jiahuan,Zhang Shiwen.Research on the current situation and countermeasures of express packaging recycling in my country [J]. China Market, 2021,(28):178-179.

[4] MaJ, LiuZ, ZhangD, Etal. Numerical Study on Vibration Response of Compressor Stator Blade Considering Contact Friction of Holding Ring[J]. Applied Sciences, 2023,13(11):10-16.

[5] Chen Jiale.Overall development of a large-scale propulsion screw automatic positioning drilling machine [D]. Tianjin: Tianjin University of Technology, 2023.

[6] Fang Chunyan.The current situation and development strategies of express packaging waste recycling [J]. Science and Technology, 2016,26(15):295.

[7] Peng Xiaopeng, Li Caiyi, Shang Hua.Structure Design of a Removable and Recyclable Express Packaging box [J]. Packaging Engineering, 2022,43(17):196-202.

Viser Technology Pte. Ltd.
Mechanical Engineering Science
DOI: 10.33142/mes.v7i1.16749

Research Article Open Access

Experimental Study of Thermal Conductivity of Multilayer Cylindrical Walls

Xin JIN[1], Pei DENG[2], Minghang TAN[3], Xidan ZHANG[3], Lingzi FENG[3], Tianlong YUAN[3*]

1. Dalian Pulandian District Power Supply Company,Dalian,Liaoning,116200,China

2. Datang Guizhou Power Generation Co.,Ltd.,Guiyang,Guizhou,550000,China

3. Liaoning Provincial Key Laboratory of Energy Storage and Utilization, Yingkou Institute of Technology ,Yingkou ,Liaoning,115014,China

[*] ***Corresponding Author:*** *Tianlong YUAN, E-mail: yuantianlong@yku.edu.cn*

Abstract

Thermal conductivity is an important physical parameter in thermal equipment, in the blast furnace, rotary kiln and other equipment, multi-layer cylindrical wall is extremely important in industrial production of a thermal conductivity model, its thermal conductivity coefficient determines the ability of the cylindrical wall, which results in the existence of a large number of multi-layer cylinder thermal conductivity problems of the pitfalls. This paper focuses on the establishment of a mathematical model of the multi-layer cylinder thermal conductivity problem, by applying different voltages to the multi-layer cylinder wall, study the temperature distribution of the multi-layer cylinder wall under the conditions of natural convection and forced convection, and draw the line graphs under the conditions of natural convection and forced convection by Origin software, and finally conclude that: under the same conditions, the forced convection is significantly stronger than the natural convection; under the conditions of different voltages, the multi-layer cylinder wall under the conditions of steady state convection, the forced convection is much stronger than natural convection. Under different voltage conditions, the temperature of the multilayer cylinder wall under steady state conditions increases with the increase of voltage, which provides a strong support for the related research.

Keywords: *Multilayer cylindrical walls; Thermal conductivity; Temperature; Experiments*

1 Introduction

In thermal equipment, heat transfer is realized through the wall of the tube, so the thermal conductivity is one of the important thermal and physical parameters of the material, characterizing the ability of material heat conduction. Its thermal conductivity determines the ability of the cylinder wall, which results in the existence of a large number of multi-layer cylinder thermal conductivity problems of hidden trouble. Such as when the internal flame temperature is too high, the refractory material will occur ablation, shedding phenomenon, serious cases of red kiln, red furnace and other malicious accidents [1]. Only understand his temperature distribution, timely grasp of the distribution of temperature overheating, so as to avoid the vicious accidents caused by excessive temperature. Through experiments and software simulation to study the temperature distribution law, through experimental simulation can not only study the distribution law of the temperature curve of thermal conductivity [2]. It can also be very intuitive to see the distribution of the temperature field inside the device, which is of great significance in solving the problem of not being able to detect the damage caused by high temperature inside the cylinder wall in time.

Blast furnace is an important equipment in steel production, providing raw materials for the production of other steel products. The cost of pig iron is 50% of the production cost of the whole iron and steel combine, so reducing the cost of pig iron is an urgent task, to achieve the reduction of the cost of pig iron, it is necessary to reduce the investment in fixed capital, and one of the measures is to build a long-life blast furnace [3]. The study of multi-layer cylindrical walls has received wide attention both at home and abroad, especially in the engineering field. This structure is widely used in various industrial equipment and installations due to its special physical and mechanical properties.

Multilayer cylindrical wall structures play an important role in various types of engineering due to their unique heat transfer, thermal resistance and structural strength properties [5]. The study of the properties of multilayer cylindrical walls can help to

Received on March 15th, 2025; Accepted on April 12, 2025

improve the operational efficiency of equipment, extend the service life, and reduce the maintenance cost. At the same time, the research results can also provide theoretical basis and technical support for engineering design and manufacturing, and promote the progress and development of engineering practice; with the increasingly serious global energy shortage and environmental pollution problems, energy saving and emission reduction has become the focus of today's society [6]. The study of multilayer cylindrical wall helps to promote the innovation of energy saving and emission reduction technology. By optimizing the structure and materials of the cylinder wall, energy consumption and pollution emissions can be reduced, promoting green and sustainable development.

2 Test

2.1 Experimental setup

(1) Overall device: the multi-layer cylinder wall is divided into three layers, from the inside out is the pipe, cement pipe (high alumina cement and particle size of 3 ～ 6mm volcanic stone in accordance with the 1:1.5 evenly mixed), thermal insulation cotton (aluminum silicate ceramic fiber paper), cast as a whole;

(2) Control device: use the regulator knob to adjust the voltage value under different gears to carry out heating of the multi-layer cylinder wall at different temperatures.

(3) Measuring device: Measuring device includes multi-layer cylinder wall, two K-type thermocouples, three linear thermocouples, DM6902 temperature digital display, one-way contact regulator, smoke tube, finned single-ended single-ended heating tube (220V, 400W) and so on.

2.2 Experimental principle

According to the thermal conductivity differential equation:

$$\frac{d}{dr}\left(r\frac{dt}{dr}\right)=0 \tag{1}$$

If it is known that the radius of the inner wall is r_1 and the temperature t_1, and the radius of the outer wall is $r_2$and the temperature is t_2, the boundary conditions corresponding to Eq. (1) are $r=r_1,t=t_1;r=r_2,t=t_2$, which yields a temperature distribution of:

$$t=t_1+\frac{t_2-t_1}{ln(r_2/r_1)}ln(r/r_1) \tag{2}$$

The derivation of Eq. (2) is taken into Fourier's law and obtained as:

$$q=-\lambda\frac{\mathrm{dt}}{\mathrm{dr}}=\frac{\lambda}{r}\frac{t_1-t_2}{ln(r_2/r_1)} \tag{3}$$

The heat flow through the entire cylinder wall $\phi$is

$$\phi=2\pi r_1=\frac{2\pi\mathrm{l}\lambda(t_1-t_2)}{\ln(r_2/r_1)} \tag{4}$$

The thermal resistance of thermal conductivity through the entire cylinder wall is:

$$R=\frac{\triangle t}{\phi}=\frac{ln(r_2/r_1)}{2\pi\lambda l} \tag{5}$$

As with analyzing multilayer walls, applying the principle of superposition of series thermal resistance, the thermally conductive heat flux through a multilayer cylindrical wall can be obtained as (assuming good interlayer contact):

$$\phi=\frac{2\pi\mathrm{l}(t_1-t_4)}{ln(r_2/r_1)/\lambda_1+ln(r_3/r_2)/\lambda_2+ln(r_4/r_3)/\lambda_3} \tag{6}$$

The temperature between the layers of the wall can be obtained by thermocouple measurements, or can be calculated using theoretical formulas under the condition that the internal and external wall temperatures are known, for the nth layer of the cylindrical wall there are:

$$t_n=t_1-\frac{\phi}{2\pi l}\left(\frac{1}{\lambda_1}ln\frac{r_2}{r_1}+\frac{1}{\lambda_2}ln\frac{r_3}{r_2}+\ldots\ldots+\frac{1}{\lambda_n}ln\frac{r_n}{r_{n=1}}\right) \tag{7}$$

3Experimental Procedure

3.1Experimental operation process

(1) Multi-layer cylindrical wall temperature measurement device before work, first check whether the connection is good, plug in the power supply, slowly adjust the one-way contact regulator, so that it is adjusted to a certain value.

(2) Open the temperature digital display, observe the changes in the number of signs, when the temperature digital display readings in a minute without a significant jump in the case, identified as this time the multi-layer cylindrical wall temperature measurement device has reached thermal equilibrium.

(3) In order to record the center of the furnace chamber temperature t_0, the temperature of the inner wall of the furnace chamber t_1, the temperature of the inner wall of the cement pipe t_2, the temperature of the inner wall of the insulation cotton t_3 iron, the circle of the temperature of the inner wall of the t_4, in order to data accurately, you can carry out a number of measurements.

(4) After the end of the measurement, first of all, slowly adjust the one-way contact regulator, so that it is adjusted to zero, turn off the power switch as well as the temperature digital display meter.

3.2 Experimental data

(1) Record parameters such as ambient temperature and humidity for the day;

(2) Close doors and windows to reduce the impact of external convection on the experiment;

(3) Check the power cord equipment and plug in the power supply;

(4) Slowly adjust the voltage regulator to 50V for natural convection experiments;

(5) Record a set of data at intervals of one hour until it reaches steady state;

(6) After reaching steady state, turn on the forced

convection and measure the wind speed value of 4.2m/s;

(7) Every ten minutes, record a set of data until it reaches steady state;

(8) Sequentially adjust the regulator to 75V, 100V repeat the above operation, the experiment;

(9) Record data.

Table 1 Temperature data at **50**V

Natural Convection	t_0	t_1	t_2	t_3	t_4	time	Forced Convection	t_0	t_1	t_2	t_3	t_4	time
	21	21	21	21	21	7:45		45	38	37	24	23	17:55
	30	26	26	24	23	8:45		44	36	37	24	23	18:05
	36	30	30	26	26	9:45		42	36	36	24	23	18:15
	40	34	33	28	27	10:45		42	35	35	24	23	18:25
	42	36	35	30	28	11:45		42	34	35	24	23	18:35
	44	37	37	31	29	12:45		42	34	34	24	23	18:45
	45	38	37	32	30	13:45		41	34	34	24	23	18:55
	45	39	38	32	30	14:45		40	32	33	24	23	19:05
	46	40	39	32	30	15:45		40	32	33	24	23	19:15
	46	40	39	32	30	16:45		39	32	32	24	23	19:25
	46	40	39	32	30	17:45							

Table 2 Temperature data at **75**V

Natural Convection	t_0	t_1	t_2	t_3	t_4	time	Forced Convection	t_0	t_1	t_2	t_3	t_4	time
	21	21	22	22	20	8:10		74	59	57	35	26	18:30
	45	31	31	27	26	9:10		72	58	56	29	26	18:40
	60	42	42	34	31	10:10		70	56	54	28	25	18:50
	68	51	50	39	35	11:10		70	56	53	27	24	19:00
	71	55	54	41	36	12:10		70	55	53	25	24	19:10
	74	58	58	44	38	13:10		69	55	53	24	24	19:20
	76	63	59	45	39	14:10		69	55	53	24	23	19:30
	77	64	61	46	40	15:10		68	54	52	24	23	19:40
	78	64	62	48	40	16:10		68	54	52	24	23	19:50
	78	64	62	48	40	17:10		68	54	52	24	23	19:00
	78	64	62	48	40	18:10							

Table 3 Temperature data at **100**V

Natural Convection	t_0	t_1	t_2	t_3	t_4	time	Forced Convection	t_0	t_1	t_2	t_3	t_4	time
	21	21	21	21	21	8:55		110	86	82	35	29	19:05
	67	48	41	33	30	9:55		107	84	79	34	28	19:15
	68	64	58	43	39	10:55		105	81	77	34	28	19:25
	99	72	71	51	44	11:55		101	79	75	34	28	19:35
	106	84	78	55	47	12:55		100	77	73	33	28	19:45
	111	90	83	58	49	13:55		98	74	72	32	27	15:55
	113	93	86	61	51	14:55		96	73	70	32	27	20:05
	112	94	87	61	51	15:55		95	71	68	31	27	20:15
	112	94	88	61	51	16:55		94	71	66	31	27	20:25
	113	94	88	61	51	17:55		94	71	66	31	27	20:35
	113	94	88	61	51	18:55							

3.2 Results of the experiment

The temperatures at which 50V, 75V and 100V reached steady state were plotted as line graphs using origin and the results are shown in Figures 1～3.

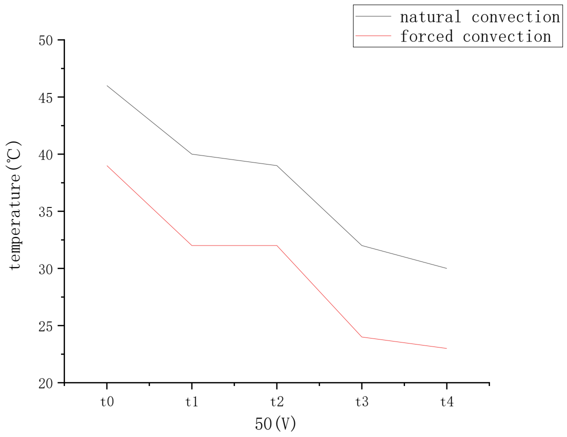

Figure 1 50V steady state values

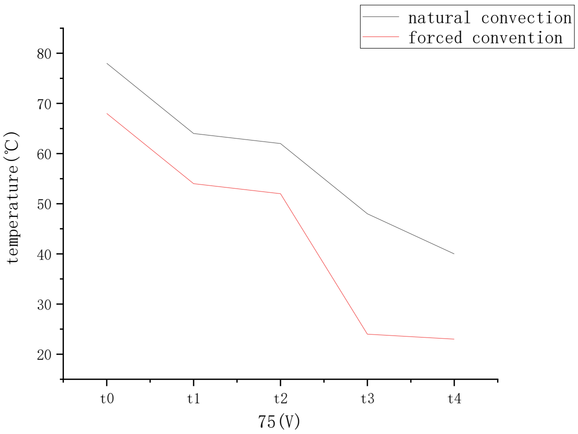

Figure 2 75V steady state values

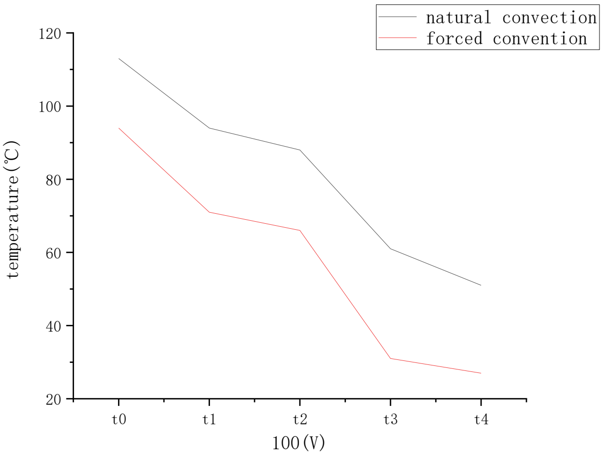

Figure 3 100V steady state values

3 Conclusion

Through the experimental results, it is found that natural convection and forced convection have similarity in temperature distribution and heat flow density in the walls of multilayer cylinders. Due to the different materials, the thermal conductivity is different. Specifically, it is shown as follows: under the same working condition, the temperature change between t_1 and t_2 in the experiment is small, and the thermal conductivity phenomenon is not obvious, and the temperature change between t_2 and t_3 is large, and the thermal conductivity phenomenon is obvious; under the same condition, the forced convection is obviously stronger than the natural convection; under the condition of different voltages, the higher the voltage is, the higher the temperature under the steady state condition is also the higher one.

Fund Projects: The Natural Science Foundation of Liaoning Province of China (Grant No. 2023-MSLH-314), and the 2024 Yingkou Institute of Technology Campus level Scientific Research Project (FDL202408); The Foundation of Liaoning Provincial Key Laboratory of Energy Storage and Utilization(GrantNo.CNNK202406), Yingkou Institute of Technology campus level research project—Development of food additive supercritical extraction equipment and fluid transmission system research(Grant No.HX202427).

References

[1] WANG Yanjun, QIU Xunong, WANG Dongliang. Determination of inner wall temperature of multilayer cylindrical wall with variable thermal conductivity [J]. Shandong Building Materials, 1998,(3):48-49.

[2] LU Xuechang. Calculation of non-stationary steady state heat transfer in multi-layer cylinders [D]. Shenyang: Northeastern University, 2008.

[3] MailyanD ,Trufanova E .Planning of Multilayer Cylindrical Wall Reservoirs [J]. Procedia Engineering, 2016,150(C):1926-1935.

[4] Ding Lei. Research on rolling technology of variable thickness plate and its thickness control model [D]. Taiyuan: Taiyuan University of Science and Technology, 2011.

[5] Gu Lidong, Zheng Jianwei, Shi Junlin, et al. Research on the design of heat preservation of large diameter high temperature and high pressure steam pipeline over long distance [J]. Refining Technology and Engineering, 2023.

Viser Technology Pte. Ltd.
Mechanical Engineering Science
DOI: 10.33142/mes.v7i1.16750

Research Article Open Access

Lightweight Design of a Certain Type of Dump Truck Frame

Chuanqi LI, Jian ZOU [*], Yongjie LI, Yingwen REN, Xinxing YU
Yingkou Institute of Technology, Yingkou, Liaoning, 115014, China

[*] ***Corresponding Author:*** *Jian ZOU, E-mail: zoujianqw@163.com*

Abstract

With the rapid growth of China's economic strength, the demand and market share are also constantly increasing. The number of cars is rapidly increasing, and a large amount of fuel is consumed as a result. The massive release of vehicle exhaust seriously damages the natural environment, and the environmental crisis is becoming increasingly serious. This article follows the principles of improving fuel efficiency, reducing emissions, and enhancing vehicle performance. Using NX 12.0 software, a three-dimensional model of a certain type of dump truck frame is constructed based on actual parameters. ANSYS Workbench is used to simplify the geometric model, mesh division, and material definition, and a finite element model is constructed. Obtain the structural performance and natural vibration characteristics of the original chassis under four typical working conditions: bending, torsion, lifting, and unloading, through static analysis and modal analysis. On this basis, the dimensions of the components that bear less load on the original frame were optimized, and the topology of the second crossbeam and rear end corner of the subframe that bear less load on the original frame was optimized to obtain a new frame. The new frame of the dump truck underwent secondary static analysis and modal analysis, and it was found that the weight of the new frame decreased by 41.03 kg, successfully reducing the weight of the frame by 4.38%, improving the vehicle's handling and stability, and extending its service life.

Keywords: *Dump truck frame; Lightweight design; static analysis*

1 Introduction

With the rapid development of the automotive industry and the continuous improvement of China's transportation system, the transportation industry in China has also shown a clear trend of development. Compared with ordinary trucks, dump trucks not only can load goods, but also have the advantage of mechanized cargo loading and unloading, effectively reducing the time spent on cargo loading and unloading, saving the labor force of workers, and improving worker efficiency. dump trucks have gradually become an important tool for cargo transportation.

With the increasingly strict environmental regulations, the market's demand for efficient and environmentally friendly transportation vehicles has increased, and enterprises need to constantly innovate to meet these needs. The exploration of lightweight optimization of vehicle frames often involves various aspects such as analysis and optimization of the frame structure. Through experimental simulation methods such as static analysis and modal analysis, the optimal optimization scheme is selected to improve the frame stiffness and durability, ensuring the safety and reliability of the vehicle under various working conditions.

The lightweight design of dump truck frames not only improves the performance and economy of vehicles, helps enterprises improve their technological level, meet new market requirements, enhance their market adaptability and innovation capabilities, but also has important significance for environmental protection, technological progress, and industry competition.

2 Creation of Finite Element Model for Vehicle Frame

2.1 Creation of 3D model of vehicle frame

This article selects a certain model of dump truck frame, which is mainly composed of two parts: the main frame and the sub frame. The main frame is usually fixed above the wheels by the suspension device, front axle, and rear axle support, playing a role in supporting and connecting various components of the vehicle. It not only plays a key role in maintaining the relative positional accuracy of all components, but also bears the impact of various loads from internal and external sources. Therefore, the frame must have sufficient strength and rigidity to withstand the heavy weight of the vehicle and the impact force transmitted through the wheels. As shown in Figure 1, the main frame mainly consists of seven crossbeams and two longitudinal beams, with the longitudinal beams being the main load-bearing parts. The crossbeam is mainly fastened to the corresponding

Received on February 7th, 2025; Accepted on March 4th, 2025

position of the longitudinal beam through fixed seats at both ends, helping the longitudinal beam to share various loads and increase the torsional strength of the frame. In addition, there are carriage lifting mechanisms installed at both ends of the main frame, which are connected to the subframe. When the lifting mechanism of the carriage rises or falls, it will drive the subframe to rise or fall, in order to achieve the purpose of self dumping of the vehicle.

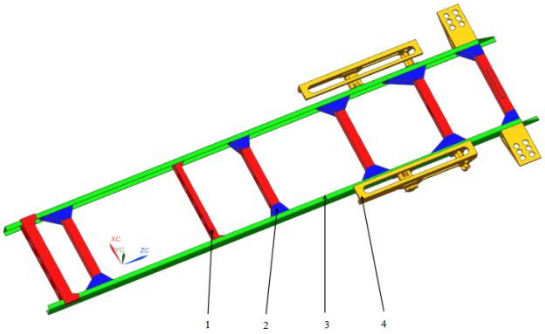

1-Beam; 2-Fixed seat; 3-Longitudinal beam; 4-Car lifting mechanism

Figure 1 Simplified Model of Main Frame

The subframe is mainly composed of two longitudinal beams and six transverse beams. The connection method between the transverse beams and the longitudinal beams is the same as that of the main frame, and they are fixed to the corresponding positions of the longitudinal beams through fixed seats, as shown in Figure 2. Unlike the main frame, the longitudinal beam and crossbeam at the rear end of the subframe, as well as the fastening of the left and right structures, use corner crossbeam components to make the rear end structure more tightly connected. The rear crossbeam of the car is welded with six sets of connecting buckles and suspended supports at both ends, which are used to connect other hanging structures of the car.

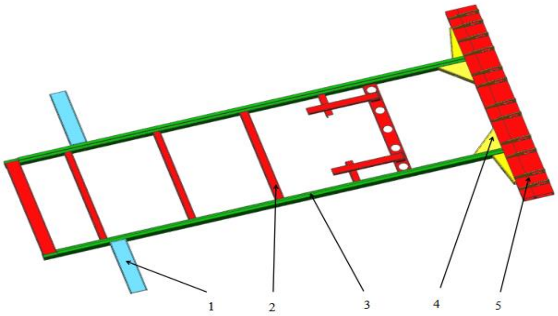

1-Support; 2-Beam; 3-Longitudinal Beam; 4-Corner Crossbeam Component; 5-Connecting Ring Buckle

Figure 2 Simplified model of subframe

When conducting static and modal analysis on the frame model of this type of dump truck, the difference between the constructed 3D model and the model used for finite element analysis is a key factor that causes the analysis results to be inconsistent with the actual situation. Therefore, this article uses NX 12.0 3D drawing software to construct the 3D model of the dump truck frame, following the principle of reasonable simplification, that is, to accurately establish the 3D model of the parts that have a greater impact on finite element analysis as close as possible to the actual situation, ignoring small details such as small holes or groove structures; Discard components that do not bear the force on the frame or have a small impact on the frame load; Neglecting unnecessary rounded corners and small chamfers can reduce the number of elements and nodes in the finite element model, improve the calculation speed of the model, reduce the difficulty of finite element analysis of the frame, and reduce the computation time for obtaining results. The simplified overall structural model of the dump truck frame is shown in Figure 3.

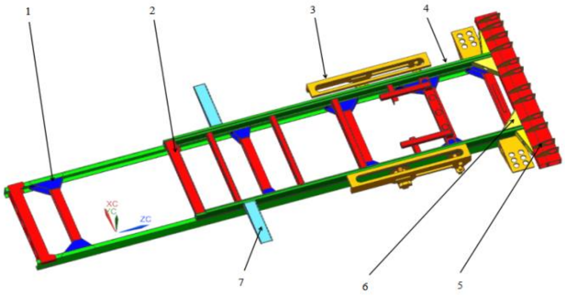

1-Fixed Seat; 2-Beam; 3 -Lifting Structure; 4-Longitudinal Beam; 5-Connection; 6-Corner Crossbeam Component; 7-support

Figure 3 Frame model of chassis

2.2 Grid division and material assignment

In the finite element analysis of this article, considering the size and structural details of the frame, a shell element size of 8 mm is assigned to the frame. For complex parts such as the contact between the crossbeam and longitudinal beam, taking into account various detailed features such as the edge position of the frame and the contact points of each component, the unit size for the above positions is set to 4 mm. In addition, in order to ensure the accuracy and computational efficiency of the finite element analysis results, this paper omitted the lifting device of the frame when meshing the frame, and only retained the main frame and sub frame. Based on this, the various components of the frame were meshed, and the corresponding connection relationships between each component were established, constructing a mesh meshing model for the frame. According to the above parameters, a total of 23345 grid cells and 59406 nodes were generated in this article's grid division.

The material of the selected dump truck frame in this article is B610L, which is a low-alloy steel known for its high strength and good weldability. A series of physical properties are shown in Table 1.

Table 1 Material parameter table

Material	Elastic modulus(MPa)	Poisson's ratio	Density(t/mm^3)	Yield limit(MPa)
B610L	2.1×105	0.3	7.89×10-9	500

3 Static Analysis of a Aertain Aype of Aump Aruck Arame

In the selection of load data for the original chassis, the total weight of the cab assembly is 450 kg, with a gravity of 4410 N; The powertrain integrated with engine, clutch, etc. has a mass of 660 kg and a measured gravity of 6468 N; When the mass of the cargo container is combined with the maximum load specified in its design, the accumulated mass obtained is 9530 kg, and the gravity is 93394 N. Among them, in order to make the calculation results more realistic, ensure its functional capability and operational safety, the gravity acceleration value is selected as 9.8 N/kg during gravity calculation.

3.1 Bending condition

3.1.1 Load and constraints

The gravity of the cab assembly and the gravity exerted by the powertrain cab assembly and powertrain are applied as concentrated loads at their respective centers of mass. On the contrary, the influence of gravity from the cargo box assembly and the goods it carries on the integrity of the frame structure is more dispersed, and is loaded onto the left and right longitudinal beams of the frame in a uniformly distributed load form. By adopting a card based approach, the gravity of the chassis itself was included in the analysis, which improved the accuracy of the simulation.

As the frame is connected to the axle through a suspension assembly located on the side of the main frame longitudinal beam, its translational motion in the X, Y, and Z directions can be restricted by designated nodes along the symmetrical centerline. Therefore, displacement constraints are applied at the six pairs of axles on the main frame, and loads are applied at the center of mass of the corresponding positions of the cab, power cab assembly, and powertrain. Apply constraints to the original frame model as shown in Figure 4.

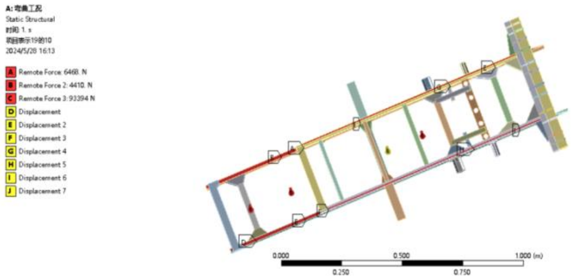

Figure 4 Original frame load and constraints under bending conditions

3.1.2 Result analysis

As shown in Figure 5, after observing and studying the stress distribution of the original frame under bending conditions, it is evident that the stress is mainly concentrated in the middle suspension position of the frame and at the connections with various suspension components. The maximum recorded stress value is 229.1 MPa, while the stress values in other important areas are mainly 203.6 MPa. Considering the smooth operation of dump trucks under these conditions, the probability of variability, transient properties, and load uncertainty is relatively small, therefore the safety factor is set to 2. The allowable stress value of the original frame under this specific condition is determined to be 250.0 MPa. Since the maximum stress value is lower than the allowable stress value, it can be concluded that the original frame meets the loading requirements of the dump truck, thus proving its sufficient strength.

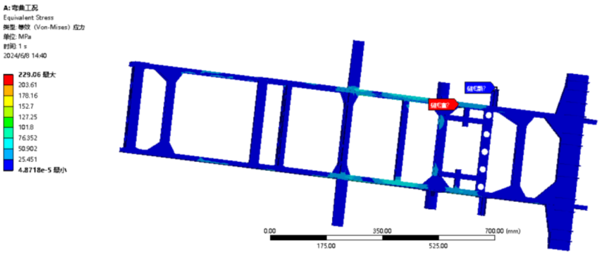

Figure 5 Stress distribution diagram of the original chassis under bending conditions

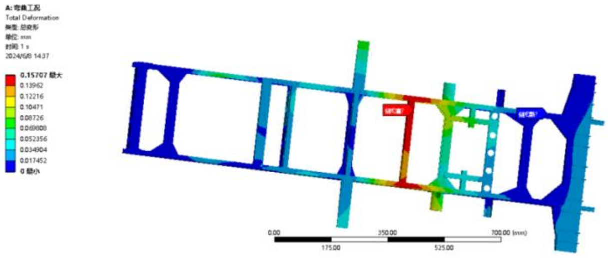

Figure 6 Stress distribution diagram of the original chassis under bending conditions

By observing and studying the dimensional deformation diagram of the original frame under bending conditions, it can be seen that the area with large deformation is located in the middle and surrounding areas of the subframe, with the greatest impact on the fourth crossbeam of the subframe, with a displacement of approximately 0.1571 mm. The rest of the frame has basically no deformation, so the frame stiffness is good.

3.2 Twisting condition

Twisting condition refers to the situation where a fully loaded dump truck travels through rugged and complex road environments at a certain speed. In this case, the wheels of the dump truck may encounter protruding obstacles or concave pits, causing at least one of the wheels to be suspended in mid air. The occurrence of this event will result in uneven force distribution on the original frame when affected, leading to a certain degree of twisting of the vehicle. When the vehicle is fully loaded with goods, the main load on the original frame comes from the weight of the goods, and the overall center of gravity is mainly located at the rear of the vehicle. The suspension of the rear wheels of the dump truck has a significant impact on the frame. Therefore, this section selects the case of left rear wheel suspension for the strength analysis of the frame.

3.2.1 Load and constraints

As shown in Figure 6, the left rear wheel is not constrained, and maintaining the same constraints as the bending condition at other positions can ensure the consistency of the simulation, thus enabling a more comprehensive evaluation of the performance of the frame under different operating conditions. According to the above description, displacement constraints are applied to the first four pairs of axles and the last two pairs of right axles.

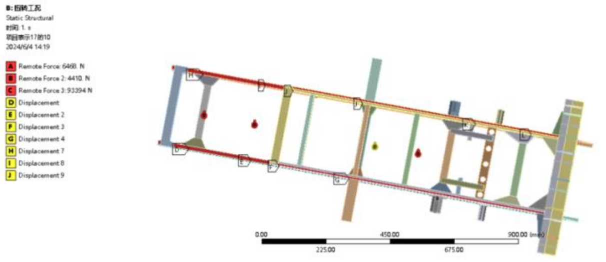

Figure 6 Load and constraints of the original frame under torsional conditions

3.2.2 Result analysis

As shown in Figure 7, after observing and studying the stress distribution of the original frame under torsional conditions, it can be seen that when the frame undergoes torsion, the sixth crossbeam of the main frame and its surrounding area, as well as the left side carriage support part and its surrounding area of the subframe, are greatly affected, with a maximum stress of 332.1 MPa. Considering the high variability, transience, and uncertainty of the load on the dump truck frame under this operating condition, in order to provide higher safety assurance, the safety factor is set to 1.5. Therefore, the allowable stress value of the original frame under this specific condition is determined to be 333.3 MPa. Since the maximum stress value obtained from the calculation is lower than the allowable stress value, it can be concluded that the original frame meets the torsional load requirements of the dump truck, thus proving its sufficient strength.

As shown in Figure 8, through the analysis of the deformation trend chart of the original frame under torsional conditions, it can be seen that when the left rear wheel of the dump truck is suspended, the deformation of the left rear part of the frame is the largest, with a deformation value of about 2.16 mm. This deformation gradually decreases towards the periphery, while the deformation of other parts is relatively small. Overall, under torsional conditions, the overall torsional stiffness of the chassis is relatively high, which means that when the model dump truck is fully loaded and driving on rough roads, the load-bearing capacity of the chassis is relatively weak.

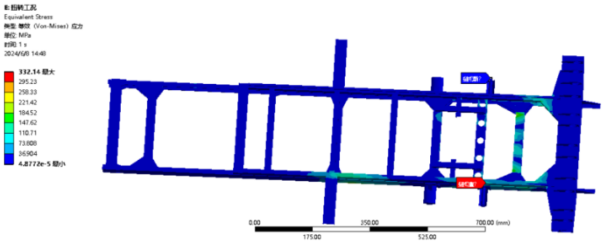

Figure 7 Stress distribution diagram of the original frame under torsional working condition

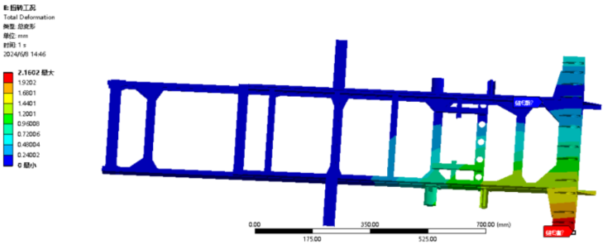

Figure 8 Deformation diagram of the original frame size under torsional condition

3.3 Lifting condition

During the lifting process of the dump truck, significant changes occur in the dynamics and forces acting on the frame. At the beginning of the lifting phase, load conditions different from those in the static or motion state of the vehicle were introduced. When the cargo box starts to lift, its weight and the force related to the lifting action are transmitted to the frame through specific connections, and the position and type of these connections determine how the lifting force is distributed on the frame. Similarly, a tilting mechanism that allows the container to rotate and tilt is also connected to the frame and container. By understanding the precise connection points and methods between the lifting device, tilting mechanism, and frame, necessary loads and constraints can be accurately applied to the frame model. This section selects the initial state of the frame during lifting for research.

3.3.1 Load and Constraints

When conducting structural analysis on the frame of this model of dump truck, loads that simulate real-world conditions are usually applied. In this case, the cab assembly consisting of the cab and related structures, the powertrain consisting of the engine and other power transmission components, and the assembly of the cargo box and its payload are considered as concentrated forces. These forces are applied at specific points corresponding to the center of mass of these components within the frame model. By using a card based method, the gravity of the frame itself was included in the analysis, and gravity acceleration was applied in the negative Y-axis direction of the frame model, which improved the accuracy of the simulation.When the cargo box is lifted, specific nodes representing the interaction with the ground on the frame model need to be constrained to prevent the frame from translating in different directions.

Thus, displacement constraints are applied at the center of mass of the six pairs of axles on the main frame, the cab, and the powertrain cab assembly, as shown in Figure 9.

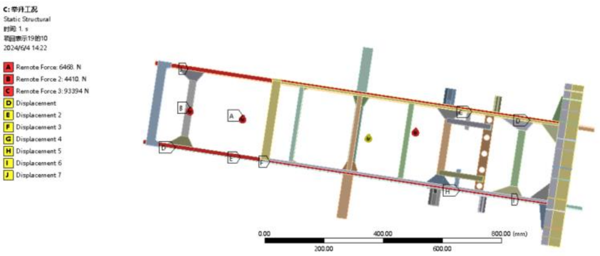

Figure 9 Load and constraints of the original frame under lifting conditions

3.3.2 Result analysis

As shown in Figure 10, after observing and studying the stress distribution map of the original chassis under lifting conditions, it can be found that during lifting, the structural integrity of the dump truck chassis is subjected to the highest stress in specific areas, and the maximum stress is mainly concentrated in the middle part of the chassis and the area leading to the rear, with a maximum stress value of 229.1 MPa. Considering the high variability, transience, and uncertainty of the load on the dump truck under this operating condition, in order to provide higher safety assurance, the safety factor is set to 1.5. Therefore, the allowable stress value of the original frame under this specific condition is determined to be 333.3 MPa. The maximum stress value obtained from finite element analysis is lower than the allowable stress value calculated theoretically. Therefore, it can be concluded that the original frame meets the requirements of this type of dump truck under lifting conditions, thus proving that the frame strength is sufficient.

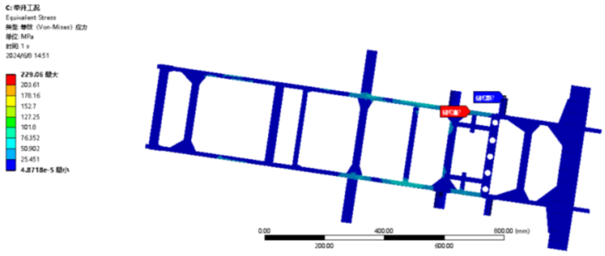

Figure 10 Stress distribution diagram of the original frame under lifting conditions

During the lifting process, the deformation of the dump truck frame is not uniform throughout its entire length. The middle part of the frame usually bears the load transmitted from the cargo box through the lifting mechanism, and its degree of deformation is also the highest. The maximum deformation occurring at the fourth crossbeam of the subframe indicates that this area is a critical point in the structure, with a maximum deformation of approximately 0.1571 mm. This may be due to the concentration of forces or the relative weakness of the crossbeam compared to other components in the frame.

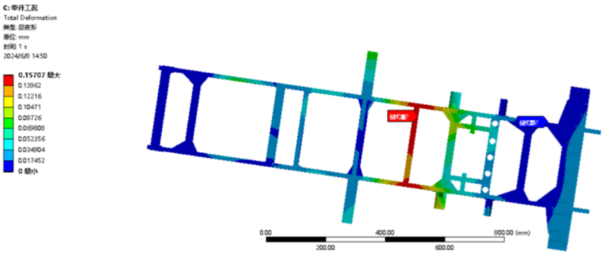

Figure 11 Deformation diagram of the original frame size under lifting conditions

3.4 Unloading condition

Unloading condition refers to the situation where, when the cargo reaches a critical state where it is about to slide, the weight of the cargo exerts a lever effect at the connection point between the frame, lifting device, and tilting mechanism due to the movement of the cargo's center of mass, applying a unique load to the frame. The specific angle for unloading the static angle of the dump truck frame of this model is 45 degrees., The typical situation where goods are ready to slide out of the cargo box. Therefore, this section will simulate the real-life scenario of the dumping process based on the above theoretical basis.

3.4.1 Load and Constraints

The cab assembly, powertrain, cargo box, and their payload assembly are considered as concentrated forces. These forces are applied at specific points corresponding to the center of mass of these components within the frame model. By using a card based method, the gravity of the frame itself is included in the analysis, and gravity acceleration is applied in the negative Y-axis direction of the frame model.When in the unloading condition, the dump truck should be stationary on the road surface, with the same constraints as the lifting condition. Displacement constraints should be applied at the six pairs of axles on the main frame, the center of mass of the cab, and the powertrain assembly, as shown in Figure 12.

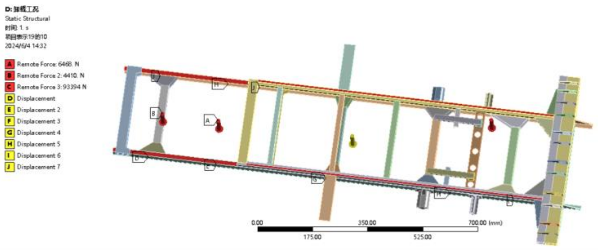

Figure 12 Load and constraints of the original chassis under unloading conditions

3.4.2 Result analysis

As shown in Figure 13,according to the analysis of the stress contour diagram of the original frame under the unloading condition, when the dump truck is in the unloading condition, the stress is mainly concentrated in the middle of the frame and some areas later, and the maximum stress value is 269.0 MPa. Considering the variability, transience and uncertainty of the load on the dump truck under this working condition, in order to provide higher safety guarantee, the value of the safety factor is 1.5, so that the allowable stress value of the original frame under this specific condition is determined to be 333.3 MPa. The maximum stress value obtained by finite element analysis is lower than the allowable stress value calculated theoretically, so it can be concluded that the original frame meets the requirements of this type of dump truck under unloading conditions, so as to prove that the frame strength is sufficient.

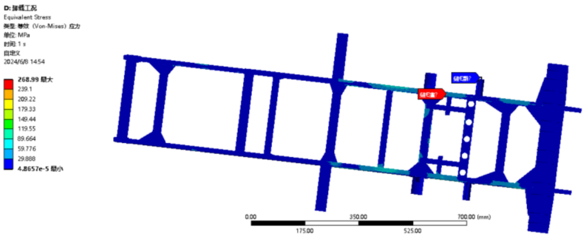

Figure 13 Stress distribution diagram of the original frame under unloading conditions

In the unloading condition, the container is only connected to the lifting device and the tilt seat, and the center of mass of the load is shifted backwards. As shown in Figure 13,through the observation and study of the frame deformation diagram under this working condition, it can be found that the main deformation area of the frame is concentrated in the fourth cross beam and later parts of the subframe, and the maximum size deformation is about 0.1524 mm, and the deformation extends backward and gradually decreases, so it can be analyzed that the stiffness of the frame is appropriate.

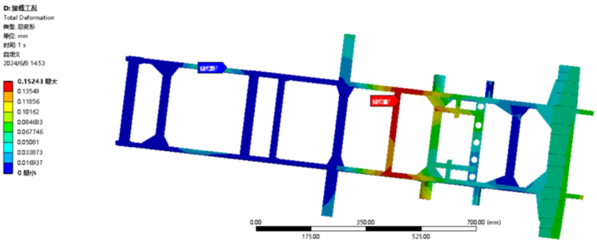

Figure 14 Deformation diagram of the original frame size under unloading conditions

As shown in Table 2, according to the actual working conditions of a certain type of dump truck, four typical working conditions of bending, torsion, lifting and unloading were selected, and the original frame of the dump truck was analyzed by finite elements. The bending and torsional conditions test the frame's ability to withstand stresses and handle complex road conditions, while the lifting and unloading conditions simulate the direct forces encountered during loading and unloading operations. The results of the analysis show that the strength and stiffness of the frame meet the standard regardless of the working conditions. It is important to note that the maximum stress under torsional effect is close to the allowable stress limit. If this continues for an extended period of time, the frame may operate within the range of material fatigue or structural failure, creating a safety hazard.

Table 2 Analysis results of the frame under different operating conditions

Operating conditions	Allowable stress (MPa)	Frame maximum stress (MPa)	Safety	Strength check
Curved	250.0	229.1	2	Qualified
Torsion	333.3	332.1	1.5	Qualified
Lifting	333.3	229.1	1.5	Qualified
Unload	333.3	269.0	1.5	Qualified

4 Optimized Design of a Certain Type of Dump Truck Frame

4.1 Frame topology optimization design

After completing the stiffness evaluation of the frame under four working conditions, it is found that the front end of the frame, that is, the cab assembly, the powertrain range is less stressed and the deformation is not obvious, so the second cross member of the subframe and the two parts of the rear side end angle in this area are selected for topology optimization design.

4.1.1 The second crosshead is optimized

From the stress analysis and deformation analysis of the above four working conditions, it can be seen that the stress and deformation of the second cross beam of the subframe are the largest under the lifting condition, and the stress value is 25.0 MPa, so the deformation and stress simulation results of the second cross beam of the subframe in this working condition are input into the Workbench structural optimization module, the two ends of the subframe are applied fixed constraints, the upper end is stressed, the optimization target is set to retain 60% of the front axle mass, and the restriction area and the optimization area are shown in Figure 15.

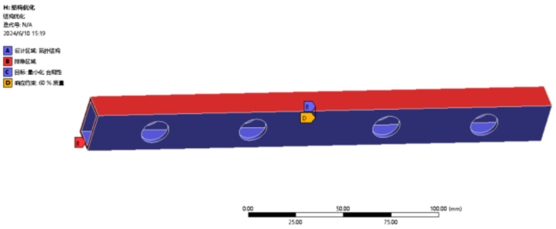

Figure 15 Second beam structural constraints

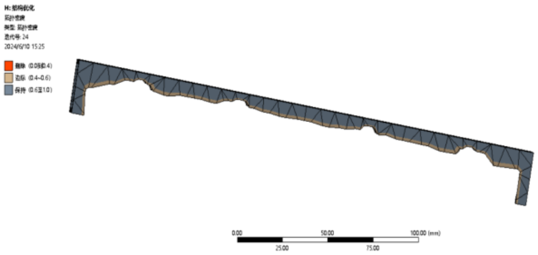

Figure 16 Optimization results of the second crossbeam

The second cross member of the subframe is placed under the defined load and constraint conditions, and then the topology optimization results of the structure in a specific scenario are calculated, as shown in Figure 16.According to the topology optimization result of the second cross beam of the subframe, the structural design of the original component is carried out again, as shown in Figure 17.

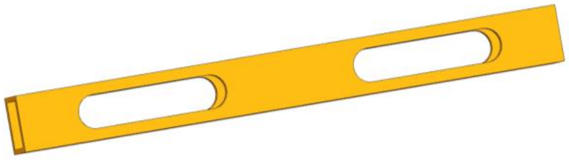

Figure 17 The structure of the second beam is optimized

4.1.2 Optimized rear end angle

Therefore, the simulation results of the rear end angle in this case are input into the Workbench structural optimization module, and a fixed constraint is applied to one end and a stress is applied to the upper end, and the optimization goal is set to retain 60% of the front axle mass, and the restricted area and optimization area are shown in Figure 18.

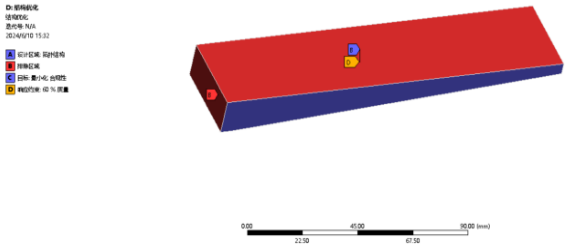

Figure 18 Rear end angle structure constraints

The virtual model of the rear end angle is placed under the above-defined loads and constraints, and then the topology optimization results of the structure in a specific scenario are solved, as shown in Figure 19.According to the results of the topology optimization of the rear end angle, the structural design of the original component is re-designed, as shown in Figure 20.

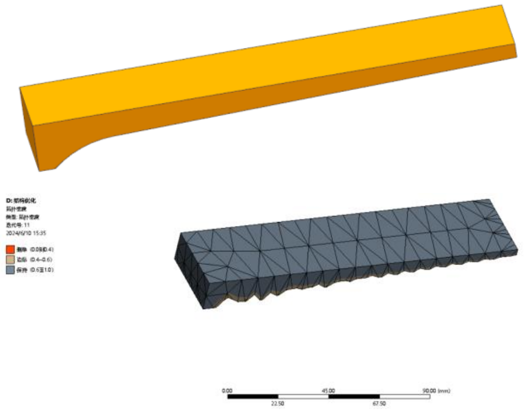

Figure 19 Result of the optimization of the rear side end angle

4.2 Optimised frame size

Through the query of literature and data, it can be obtained that the thickness of the plate of the frame of this type of dump truck produced by the manufacturer selected in this paper is 4 mm~12 mm. Combined with the above theory and analysis results, some parts of the main frame and subframe were selected for size optimization design, and the specific parameter changes are shown in Table 3.

Table 3 Size parameter optimization table

Optimize parts	Initial value(mm)	Optimize the value(mm)
Main frame rails	7	6
Main frame beam	6	4
Subframe rail	5	4.5
Subframe beam	6	4
Liners	6.5	5
Connecting plates	8	6

After the optimized design of the frame, it was found that the mass of the new frame was 895.77 kg, which was 41.03 kg less than the 936.80 kg of the original frame, a decrease of about 4.38%, which indicated that the improvement applied to the frame structure had successfully realized the lightweight design and did not affect the integrity of the frame structure of the dump truck.

4.3 Optimized static analysis of the rear frame

The stress distribution of the improved frame is viewed according to the above dimensional optimization and component optimization, and the results are shown in Figure 21～24.

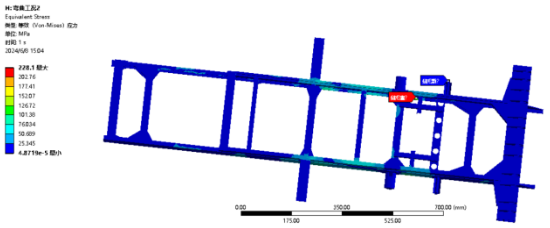

Figure 21 Stress contour of bending condition after optimization

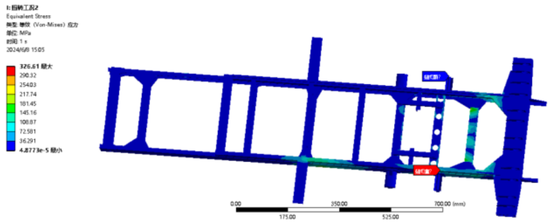

Figure 22 Stress contour diagram of torsion condition after optimization

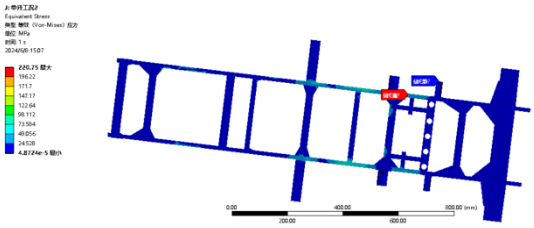

Figure 23 Stress contour diagram of the optimized lifting condition

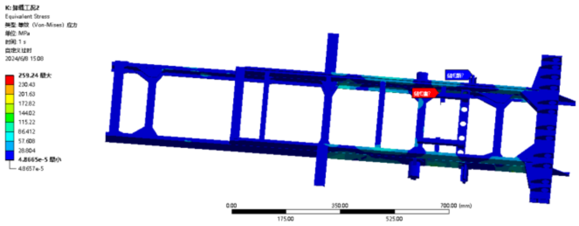

Figure 24 Stress contour diagram of unloading condition after optimization

Table 4 Comparison table of stress values under different working conditions before and after improvement

Operating conditions	Before optimizing the maximum stress(MPa)	Maximum stress after optimization(MPa)	Safety
Curved	229.1	228.1	2
Torsion	332.1	326.6	1.5
Lifting	229.1	220.8	1.5
Unload	269.0	259.2	1.5

By observing and analyzing the stress analysis diagram of the improved frame under different working conditions, it can be seen that the maximum stress area under the four working conditions is basically unchanged compared with before optimization, but the values are reduced to different degrees, the value under the bending condition becomes 228.1 MPa, the value under the torsion condition changes from 332.1 MPa to 326.6 MPa, the value decreases by 8.3 MPa under the lifting condition, and the maximum stress value decreases to 259.2 MPa under the unloading condition. And the improved frame meets the strength check under different working conditions. Table 4 compares the optimization parameters.

5 Conclusion

In this paper, a dump truck frame was taken as the research object, NX 12.0 3D software was used to construct a 3D model of the frame according to the actual parameters, and the static analysis was carried out by importing ANSYS Workbench analysis software, and the original frame structure was optimized based on this. The static analysis of the optimized frame was carried out, which successfully reduced the weight of the frame, improved the handling and stability of the vehicle, and extended its service life.

(1) The 3D model of the frame was constructed using NX 12.0 3D software according to the actual parameters, and the geometric model was reasonably simplified after importing the ANSYS Workbench analysis software, and then the meshing was carried out, and a total of 23,345 mesh elements and 59,406 nodes were generated, and the material was defined as B610L, and the finite element model of the frame was established.

(2) The static analysis of the frame was carried out under four typical working conditions: bending, torsion, lifting and unloading, and the stress contours and deformation contours under each working condition were obtained. The results show that the original frame has better strength and stiffness under four working conditions: bending, torsion, lifting and unloading, while the stress concentration is obvious under torsional conditions, and the maximum stress is close to the yield limit of the material.

(3) Based on the results of static analysis and modal analysis of the original frame, the size of the components with small load on the original frame was optimized, and the structure of the original frame was optimized by improving the connection mode and adding weight reduction holes. According to the above description, the 3D design of the optimized frame was completed, and the static analysis of the optimized frame was carried out. The results show that the structural performance of the optimized frame is more superior, and the maximum stress under each condition is significantly reduced, and it is lower than the material yield limit. At the same time, the total mass of the optimized frame has been significantly reduced by 4.38%, and the fuel economy of the whole vehicle has been improved.

References

[1] Chen Y, Zhu F. The Finite Element Analysis and the Optimization Design of the Yj3128-type Dump Truck's Sub-Frames Based on ANSYS[J]. Procedia Earth and Planetary Science, 2011(2):133-138.

[2] Ren Y, Yu Y, Zhao B, et al.Finite Element Analysis and Optimal Design for the Frame of SX360 Dump Trucks [J]. Procedia Engineering, 2017(174):638-647.

[3] Chao G, Zhiyuan L, Tianfeng M, et al.Strength analysis and optimization of three-bridge rigid frame for mining dump truck using finite element stress linearization method[J]. Journal of Physics:Conference Series,2022,2343(1):165-168.

[4] Huang Lijun, Wan Mingjun, Gao Zhigang. Lightweight design of a truck frame based on ANSYS Workbench [J]. Science & Technology Wind, 2021(19):18-21,24.

[5] Liu Qiang, Geng Jinping. Research on lightweight design and numerical simulation of electric drive dump truck frame [J]. Coal Mining Machinery, 2018,39(3):84-86.

[6] Mi Chengji, Gu Zhengqi, Jian Haigen, et al. Fatigue resistance and lightweight design of frame structure of electric wheel dump truck[J]. China Mechanical Engineering, 2017, 28(20):2455-2462.

Viser Technology Pte. Ltd.
Mechanical Engineering Science
DOI: 10.33142/mes.v7i1.16751

Research Article Open Access

Structural Design and Analysis of Lower Limb Exoskeleton Robotics

Mingshuo ZHANG, Yutong LI, Sheng ZHANG, Yuanhai DING, Chuanqi LI*
Yingkou Institute of Technology, Yingkou, Liaoning, 115014, China

***Corresponding Author:** *Chuanqi LI, E-mail: a1016084773@163.com*

Abstract

With the acceleration of the global aging process and the increase of cardiovascular an cerebrovascular diseases, more and more patients are paralyzed due to accidents, so the exoskeleton robot began to appear in people's sight, and the lower limb exoskeleton robot withrehabilitation training is also favored by more and more people. In this paper, the structural designand analysis of the lower limb exoskeleton robot are carried out in view of the patients' expectation ofnormal walking. First, gait analysis and structural design of lower limb exoskeleton robot. Based onthe analysis of the walking gait of normal people, the freedom of the three key joints of the lower limbexoskeleton robot hip joint, knee joint and ankle joint is determined. at the same time, according tothe structural characteristics of each joint, the three key joints are modeled respectively, and theoverall model assembly of the lower limb exoskeleton robot is completed. Secondly, the kinematicsanalysis of the lower limb exoskeleton robot was carried out to obtain the relationship between thelinear displacement, linear speed and acceleration of each joint, so as to ensure the coordination ofthe model with the human lower limb movement. Thirdly, the static analysis of typical gait of hipjoint, knee joint and ankle joint is carried out to verify the safety of the design model under thepremise of ensuring the structural strength requirements. Finally, the parts of the model were 3Dprinted, and the rationality of the design was further verified in the process of assembling the model.

Keywords: *Exoskeleton Robots; Mechanical Structure Design; Finite Element Analysis; Motion Simulation*

1 Introduction

With the development of society, human demand for material and spiritual needs is increasing day by day. People may suffer injuries in some traffic accidents or sports, and some injuries are irreversible to the body. Spinal injuries can cause many people to be unable to carry out daily life or even walk. For example: paraplegia. Paraplegic patients generally experience paralysis of both lower limbs, sensory disorders below the corresponding plane of injury, autonomic nervous system dysfunction, and other problems. Many patients may become bedridden due to complications caused by not actively implementing scientific and effective treatment plans, and rely entirely on the help of others to complete daily life. With the development of science and technology, more and more rehabilitation training robots have entered rehabilitation centers, and the development of such robots has given hope to patients and their families. The main users of existing lower limb exoskeleton rehabilitation robots include postoperative patients, elderly people, chronic diseases, etc. Taking knee joint surgery patients as an example, if good rehabilitation training is not provided to the patients, surgical complications such as joint adhesion and stiffness may occur. With the increasing severity of China's aging problem, the elderly population will gradually face problems such as inability to take care of themselves, chronic diseases, cardiovascular diseases, etc. The rehabilitation needs of the elderly population are constantly increasing. In the near future, open training for the elderly will become one of the mainstream groups in the medical rehabilitation market.

The lower limb exoskeleton rehabilitation robot is a wearable device used for rehabilitation training, which can provide postoperative rehabilitation training for elderly and disabled patients. The lower limb exoskeleton robot not only retains the advantages of bipedal walking robots, but also utilizes the human body's main control ability and advanced sensing technology to solve traditional drawbacks such as poor walking stability and lack of walking planning ability. It not only has the effect of protecting and supporting the human body, but also can provide appropriate force compensation to the wearer through the driving device, thereby improving various indicators such as human strength.

Received on February 10, 2025; Accepted on March 15th, 2025

2 Model Establishment of Lower Limb Exoskeleton Robotics

As an auxiliary equipment for patient rehabilitation training, lower limb exoskeleton robots need to meet the requirements of analyzing the structure and movement status of healthy human bodies, while also being designed and calculated according to the principles of bionics. Based on the existing simplified model of human lower limb joints, the following conclusions can be analyzed:

The hip joint is a ball and socket joint that performs flexion, rotation, and lateral movements in the sagittal, coronal, and horizontal planes of the human body; Knee joint master's hinge joint, usually performing flexion and extension movements in the sagittal plane; The structure of the ankle joint is similar to that of the hip joint, which is also a ball and socket joint. It can flex, extend, and flip in the sagittal, coronal, and horizontal planes of the human body.

2.1 Hip joint design

As the main joint component connected to the lumbar support and lower limbs, the hip joint needs to ensure the same motion characteristics as the human body and the overall coordination of the lower limb exoskeleton robot. Therefore, in the design of the hip joint, two femoral connection plates are used to connect it to the main leg, and the joint movement is completed on the inner side of the hip joint through the cooperation of shafts and bearings. Finally, due to the limitation of wide joint flexion motion, a joint limit plate is added on its joint support frame, as shown in Figure 1.

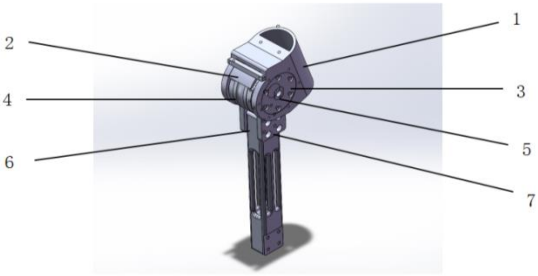

1-Hip joint support frame; 2-Hip joint limit; 3-Hip joint axis fixation plate; 4-Hip joint turbine; 5-Hip joint axis; 6-Thigh; 7-Femoral connecting plate

Figure 1 Hip joint model diagram

2.2 Knee joint design

The knee joint, as the middle part of the lower limb structure, plays a connecting role, and its movement direction is opposite to the direction of the hip joint's support frame. The fixed plate on the support frame is connected to the thigh, and the lower leg is connected to the tibia connecting plate. The lower leg can meet the rotation requirements through the cooperation of the shaft and bearing. During the movement of the knee joint, due to the angle limitation, a limit is added on the support frame of the knee joint to meet its movement requirements, as shown in Figure 2.

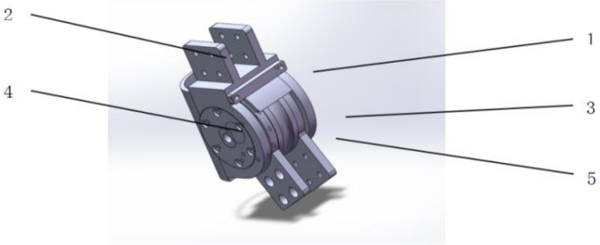

1-Knee joint limit; 2-Knee joint support frame; 3-Tibial connecting plate; 4-Knee joint axis; 5-Knee joint turbine

Figure 2 Knee joint model diagram

2.3 Ankle joint design

The ankle joint of the human body is the most complex component among the three key joints. There are many factors that need to be considered in the structural design of the ankle joint. For example, as the joint component with the smallest range of movement, the connection between the foot pedal and the ankle joint should not only rely on shafts and bearings for driving. At the same time, spring support frames need to be added at the ankle joint movement and lower leg parts. During the patient's use, springs with different elastic coefficients can be changed by restoring the situation, as shown in Figure 3.

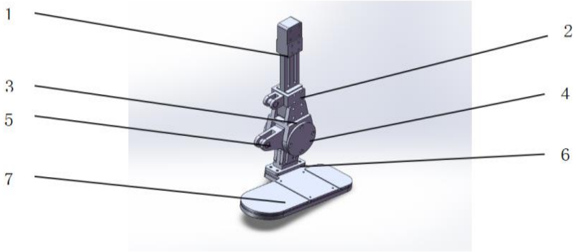

1-shank; 2-Ankle joint spring support; 3-Ankle joint support frame; 4-Ankle joint bearing end cap; 5-Ankle joint rotation axis transition plate; 6-Foot connection plate; 7-Foot board

Figure 3 Ankle joint model diagram

2.4 Overall design of lower limb exoskeleton robot

After designing three key joints, assemble them as a whole and draw the adjustable lumbar spine of the lower limb exoskeleton robot, as shown in Figure 4.

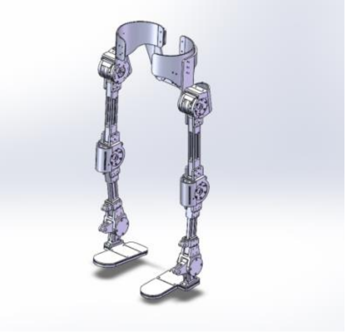

Figure 4 Overall assembly diagram

In the process of designing the joint range of motion for the entire lower limb exoskeleton robot, considering the safety of future use, limit plates are used to control the joints at each joint to ensure that they are within a reasonable range of motion and prevent secondary injuries to patients due to excessive movement amplitude, as shown in Table 1.

Table 1 Range Table of Three Joint Movement States

Joint	Motion	Safe Range(°)
Hip Joint	Swing	-5~5
	Rotate	-5~5
	Buckling	-20~35
Knee Joint	Buckling	-5~90
Ankle Joint	Buckling	-15~10

3 Kinematic Analysis of Lower Limb Exoskeleton Robot

3.1 Analysis of Hip Joint Movement

The thigh is connected to the tibial connection plate and assembled together with the hip joint, so in Solidworks' motion calculation column, motion analysis is performed through plugins. Add motor plugins to the existing joints, select the outermost vertex of the femur and the realization of the femur tibia connection plate as simulation units to generate the required corresponding result graph, as shown in Figure 5.

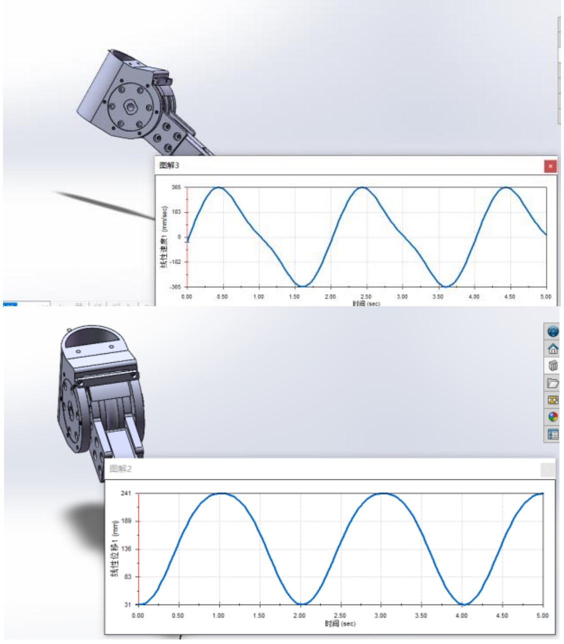

Figure 5 Linear displacement and linear velocity diagram

From the trajectory of the hip joint and calf, it can be concluded that the movement of the thigh forms a fan-shaped distribution centered on the hip joint axis. The distribution of linear displacement exhibits periodicity, with a period of 2 seconds, and the displacement reaches its highest point at 1 second. In the analysis of linear velocity graphs, the graphical pattern also exhibits periodic changes, reaching the first peak of 365 (mm/sec) at approximately 0.5 seconds and the lowest value of -365 (mm/sec) after 1 second.

3.2 Analysis of Knee Joint Movement

Due to the lack of connection with the thighs and calves, only the relevant data analysis of the tibial connection plate will be analyzed in this section. In the Motion analysis process of Solidworks, the lower end of the tibial connection plate and the upper end of the connection plate were selected as the corresponding point points to generate the required corresponding rendering, as shown in Figure 6.

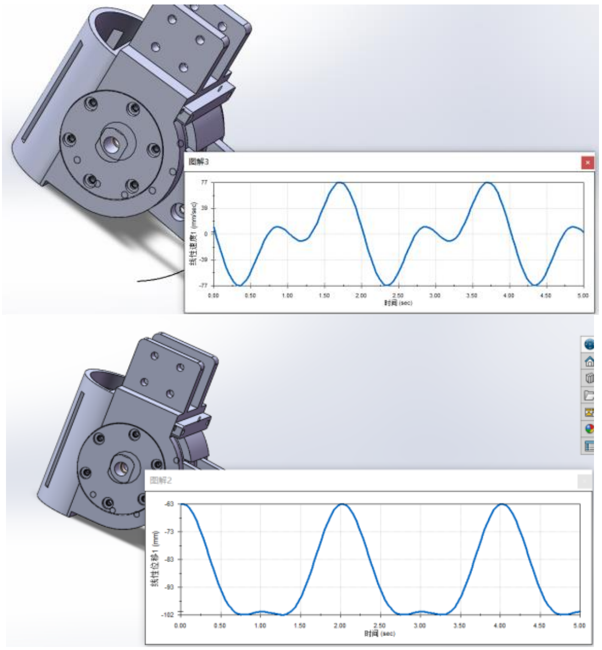

Figure 6 Linear displacement and linear velocity diagram

From the trajectory analysis diagram of the knee joint, it can be seen that the fan-shaped motion trajectory is formed at the lower end of the tibial connecting plate with the knee joint axis as the center. The diagram of linear displacement shows that during the movement of the knee joint, a cycle is formed every 2 seconds, and a peak value of -63mm is formed at the 2nd second; A continuous trough of -102mm occurs between 0.75 and 1.25 seconds, with a small peak forming at approximately -100mm at 1 second. In the analysis results of linear velocity, a period of 2 seconds is also formed. However, unlike linear displacement, linear velocity forms a slightly irregular graphical display, with a highest peak at 1.75s, approximately 77 (mm/sec), and a lowest peak at 0.3s, -77 (mm/sec).

3.3 Analysis of Ankle Joint Movement

In the analysis diagram of the ankle joint, the main research object is the movement of the foot. Therefore, in the Motion analysis process of Solidworks, the position where the front end of the foot and the foot plate are connected to the fixed plate are used as the point points in this study to generate the main analysis diagram, as shown in Figure 7.

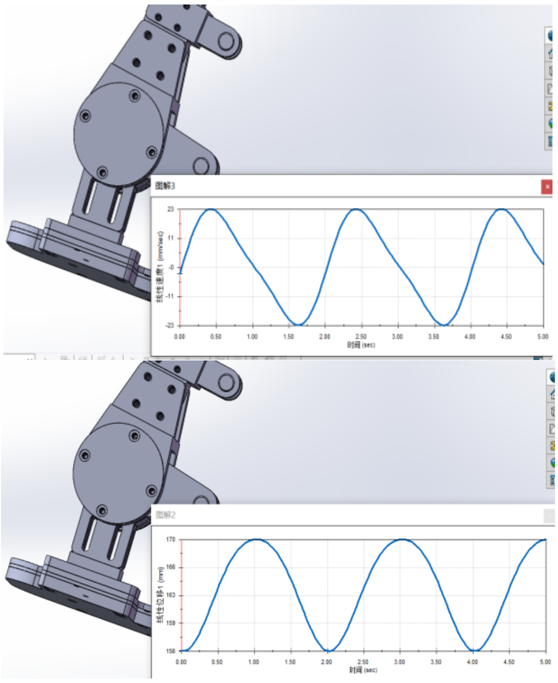

Figure 7 Linear displacement and linear velocity diagram

From the perspective of ankle joint movement trajectory, foot motion analysis is based on the selected front end of the foot as the analysis point and the ankle joint axis as the radius to generate the motion trajectory. According to the linear displacement analysis of the ankle joint, there is a periodic and regular change within 2 seconds, with only one peak and one minimum value in each cycle. The linear displacement of the highest point is 170mm, and the linear displacement of the lowest point is 156mm. The linear velocity of the ankle joint and foot varies regularly with a period of two seconds, with a maximum value of 23 (mm/sec) at around 0.4 seconds and a minimum value of -23 (mm/sec) at 1.6 seconds.

Table 2 Table of Linear Displacement and Linear Velocity Results for Three Key Joints

Joint	linear displacement (mm)			linear speed (mm/sec)		
	cycle	highest point	lowest point	cycle	highest point	lowest point
Hip Joint	2	241	31	2	365	-165
Knee Joint	2	-63	-102	2	77	-77
Ankle Joint	2	170	165	2	23	-23

4 Static Analysis of Leg Structure of Lower Limb Exoskeleton Robot

Based on the experimental subject (an adult male with a height of 175 and a weight of 60 kilograms) as a reference, this reference is used as the basic data for static analysis. Using the knee joint as the starting point of force and the hip joint as the fixed part in the static analysis of the thigh; In the static analysis of the calf, the ankle joint is used as the fixed part.The knee joint is used as the main force-applying part, and forces are applied in both horizontal and rotational directions to mimic the movement of the knee joint during human movement.At the same time, the hip and ankle joints are used to fix the thigh and calf, and the connection between the upper and lower legs of the lower-limb exoskeleton robot and the joints is used as a fixed point to ensure the restoration of the human form during movement.

4.1 Static analysis of thigh

The two sides of the thigh are symmetrically shaped, so one section serves as the connection with the knee joint, while the other end serves as the connection with the hip joint.

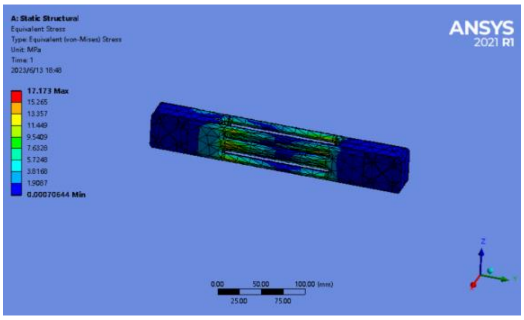

Figure 8 Distribution diagram of rotational stress

Due to the greater relative mobility of the knee joint in the human body, this analysis considers the knee joint as the main active area and adds fixed constraints to the hip joint contact area. Add a force of 90 rad/s rotating inward on the surface connecting the thigh and knee joint, and finally obtain the stress distribution diagram as shown in Figure 8. The stress distribution ranges from 0.0007 to 17.17 (MPa), with uniform stress distribution and high safety.

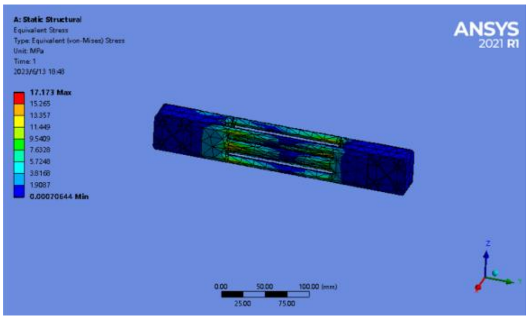

Figure 9 Horizontal stress distribution diagram

Under the condition of ensuring the hip joint connection remains unchanged, a horizontal force of 1.2 MPa is added to the knee joint force point according to the direction, and the stress distribution map is finally analyzed by software, as shown in Figure 9. The maximum stress distribution is 0.007～238.74 (MPa), with uniform stress distribution and high safety.

4.2 Static analysis of calf

The calf, like the thigh, has the knee joint as its main active joint. The connection between the lower leg and ankle joint serves as the fixed point for analysis, while the connection between the knee joint and lower leg serves as the loading point. A rotational force of 90 rad/s is applied at this point for final analysis, resulting in a stress distribution diagram as shown in Figure 10. The stress distribution is 0.001～20.00 (MPa), with uniform stress distribution and high safety.

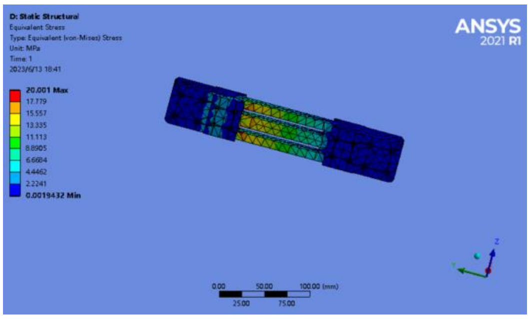

Figure 10 Distribution diagram of rotational stress

Under the condition of ensuring that the ankle joint serves as the force point without applying any loading force, a horizontal force of 12MPa is applied to the knee joint connection area, and the corresponding stress distribution diagram is finally analyzed, as shown in Figure 11. The stress distribution is 0.98-395.6 (MPa), with uniform stress distribution and high safety.

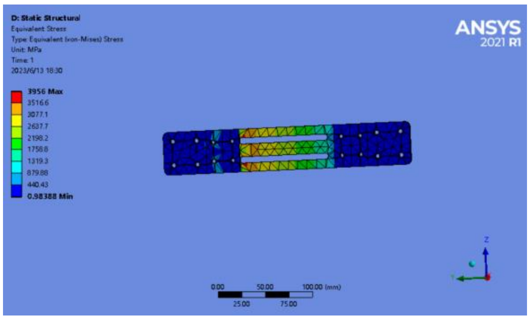

Figure 11 Horizontal stress distribution diagram

5 Additive Manufacturing of Lower Limb Exoskeleton Robots

5.1 Printing process

Save the modeled parts to STL format and use the slicing software CHITUBOX to perform slicing preprocessing, as shown in Figure 11. Set the exposure time of the bottom layer to a reasonable range value. If the exposure time is too high or too low, it will cause the printed part to be not firmly attached, resulting in printing failure.

底层光强PWM: 255 /
光强PWM: 255 /
抗锯齿: ☐
公差补偿（测试版）: ☐
底部公差补偿: ☐
打印时间补偿: ☐

切片设置

层厚: 0.050 mm
底层数: 8
曝光时间: 6.000 s
底层曝光时间: 50.000 s
过渡层数: 0
过渡类型: 线性
打印过程等待模式: 静止...
抬升前的静止时间: 0.000 s
抬升后的静止时间: 0.000 s
回程后的静止时间: 0.000 s
底层抬升距离: 5.000 + 0.000 mm
抬升距离: 5.000 + 0.000 mm
底层回程距离: 5.000 + 0.000 mm
回程距离: 5.000 + 0.000 mm
底层抬升速度: 65.000 & 0.000 mm/min
抬升速度: 65.000 & 0.000 mm/min
底层回程速度: 150.000 & 0.000 mm/min
回程速度: 150.000 & 0.000 mm/min

Figure 11 Slice parameters

During the process of placing the parts, move them into the 3D printer and raise the entire part by about 5mm to facilitate the fixation of the support body. Adjust the automatic support auxiliary material settings of the software and manually add them in areas with insufficient supportFinally, set the printing parameters for printing, as shown in Figure 13.

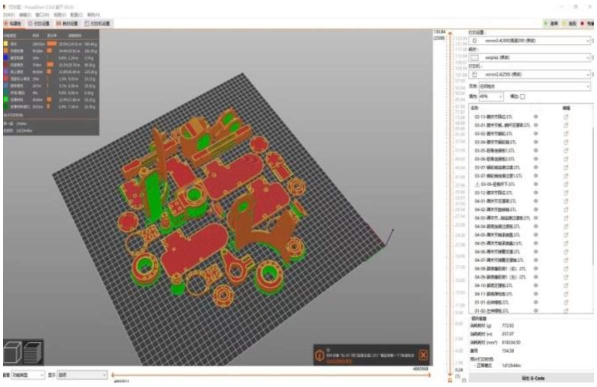

Figure 12 Model placement and printing parameters

After printing is completed, the support of the parts is removed and all parts are assembled into a complete lower limb exoskeleton robot, as shown in Figure 13.

Figure 13 Physical display

6 Conclusion

This article analyzes the design of lower limb exoskeleton robots. Through investigation and analysis of the existing social situation, it is found that there are many people in the world who need the help of exoskeletons to achieve their dreams of walking. At the same time, research on the development and production of lower limb exoskeleton robots at home and abroad has found that there are still many problems. Therefore, in this design, the lower limb exoskeleton robots will be redesigned and optimized. The following results are obtained from summarizing the entire text:

(1) Complete the analysis of normal human lower limb movement. Determine the motion status and degrees of freedom of the hip, knee, and ankle joints in a normal human body, and construct the required mechanical models based on the structural characteristics of each joint. Use Solidworks software to build and assemble the models.

(2) Conduct kinematic analysis on the three joints of the lower limb exoskeleton robot. Generate motion trajectories, linear displacements, and linear velocities of the hip, knee, and ankle joints through the motion calculation section in Solidworks software to ensure the overall motion coordination of the model.

(3) Using Ansys Workbench software, typical gait statics analysis was conducted on the hip, knee, and ankle joints, and the force analysis diagrams of the two legs were finally obtained. The safety of the model was also verified while ensuring that the strength requirements were met.

(4) Model printing of lower limb exoskeleton robots. The existing 3D printing technology was used to print the model at a 0.5x magnification and assemble it, further verifying the rationality of the model design.

Fund Projects: College Student Innovation and Entrepreneurship Project (Grant No.:S202414435026), Yingkou Institute of Technology campus level research project — Development of food additive supercritical extraction equipment and fluid transmission system research (Grant No.HX202427).

References

[1] Hybart Rachel, Ferris Daniel P. Embodiment for Robotic Lower-Limb Exoskeletons: a narrative Review. [J]. IEEE transactions on neural systems and rehabilitation engineering : a publication of the IEEE engineering in medicine and biology society, 2022,(11):22-25.

[2] Dao Quythinh, Dinh VanVuong, Trinh. Nonlinear Extended Observer-Based adrc for a lower-limb pam-based Exoskeleton [J]. actuators, 2022,11(12).111-115

[3] Sarajchi Mohammadhadi,alHares Mohamad Kenan,Sirlantzis Konstantinos. Wearable lower-limb exoskeleton for children with cerebral palsy. [J]. IEEE transactions on neural systems and rehabilitation engineering: a publication of the IEEE engineering in medicine and biology society, 2021(12):35-37.

[4] Boonekamp Francine J, Dashko Sofia,Duiker Donna,Gehrmann. Design and experimental evaluation of a minimal, Innocuous watermarking strategy to distinguish near-identical dna and rna Sequences. [J]. acssynthetic biology, 2020,9(6):35-38.

[5] Narina Ramesh, Iwaniec Marek, arawade Swapnil. Present and future of assistive robotic lower limb exoskeletons [J]. Matec web of conferences, 2022(357):46-49.

Viser Technology Pte. Ltd.
Mechanical Engineering Science
DOI: 10.33142/mes.v7i1.16752

Research Article Open Access

Lightweight Design of Front Axle Structure of a Certain Type of Automobile

Chuanqi LI, Jian ZOU *, Bing LI, Yiming LEI, Mingshuo ZHANG
Yingkou Institute of Technology, Yingkou, Liaoning, 115014, China

****Corresponding Author:*** *Jian ZOU, E-mail: zoujianqw@163.com*

Abstract
In this paper, the front axle of a certain model is taken as the research object, and the stress and deformation of the front axle under three typical working conditions are analyzed by finite element technology.Based on the simulation results, the 3D model of the front axle was optimized, and the finite element analysis of the optimized structure of the front axle under three typical working conditions was carried out to verify the correctness of the model.Finally, the fatigue tool module of ANSYS Workbench was used to analyze the fatigue life of the front axle under the optimized emergency conditions, and the feasibility of the model was verified.The analysis data shows that the design of the front axle components still has a lot of potential for lightweighting, and the weight of the front axle can be reduced by 6.73% through optimization, and the performance of the front axle can also meet the needs of use.The research conclusion has a certain reference value for the lightweight design of automobile front axle.

Keywords: *automobile front axle; structural optimization; Fatigue life*

1 Introduction

As the number of private cars continues to rise, the consumption of gasoline and its dependence on oil is also increasing, which is also leading to the increasing problem of global warming. To alleviate this, governments around the world have introduced a series of policies to limit energy efficiency and pollutant emission standards for vehicles, putting pressure on automakers. The automotive industry must continue to strive to improve its technological capabilities and develop more high-quality and environmentally friendly new automotive products.

The front axle, which is the majority of the weight of the front axle assembly, is mainly loaded at the leaf spring seat and kingpin, while the I-beam in the middle is subjected to relatively little stress. Since these areas do not use the material to its full potential, there is a huge possibility of reducing the mass. As an important part of the vehicle's suspension system, the mass reduction of the front axle can lead to more significant energy savings and emission reductions, as well as improve the operating efficiency of the whole vehicle. It is also a vital safety device in a vehicle, and it has strict requirements for its mechanical properties. In addition, the design and construction of the front axle is quite complex, and it needs to cope with various potential risk driving environments, which makes the structural lightweight not only need to meet the stability requirements under heavy loads, but also adapt to the durability standards under low load conditions. For the front axle, lightweighting is therefore an optimization task with multiple objectives and involves a complex structural design process. Thanks to the development of finite element technology and calculation tools, it has been possible to effectively optimize and interpret structural characteristics, thereby significantly reducing the development time and cost of products.The schematic diagram of the structure of the integral front axle of an automobile is shown in Figure 1.

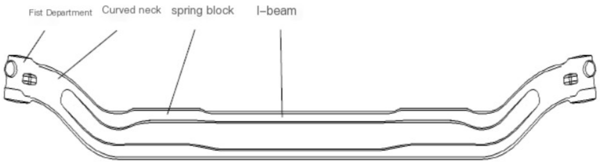

Figure 1 Schematic diagram of the front axle structure of the automoile

Due to its complex front axle construction and operating environment, the front axle of a vehicle must be high strength and durability, which often relies on the expertise of the designers and the results of extensive experimental testing. This traditional way of building is time-consuming and expensive, resulting in slow new product development and weak performance improvements. To address these challenges, a lightweight

Received on March 20, 2025; Accepted on March 18, 2025

simulation model of the front axle architecture was created using the finite element method, and its physical properties under various operating conditions were explored in depth, and then the architecture was optimized and its fatigue life was verified. Through this study, the problem of lightweight design and reliability evaluation of front axle structure is effectively solved, which provides important value for practice.

2 Finite Element Analysis of a Front Axle in a Car

2.1 Finite element model construction

The front axle model JT-TR01 is studied in this paper, and the 3D model of the front axle is established by Solidworks and imported into ANSYS Workbench software, as shown in Figure 2:

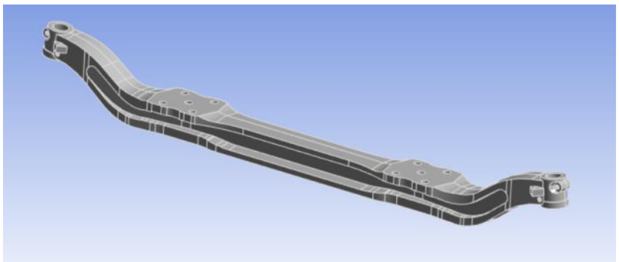

Figure 2 Finite element analysis model of the front axle

The main material of the front axle is 42CrMo, and the main parameters are shown in Table 1:

Table 1 Front axle material properties

Material	42CrM
Density	7900kg/m^3
Elastic modulus	206000MPa
Yield Limit	930MPa
Strength limit	1080MPa
Poisson's ratio	0.3

The front axle was meshed using ANSYS Workbench with a mesh size of 10 mm with a total of 113,190 elements and 175343 nodes, as shown in Figure 3.

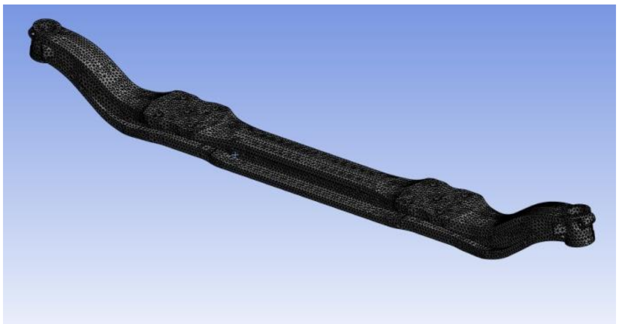

Figure 3 Meshing result graph

2.2 Finite element analysis of the front axle of a car

2.2.1 Finite element analysis under emergency braking conditions

In the event of an emergency braking of the car, the front axle will be subjected to the increased vertical load due to the forward movement of the overall center of mass and the horizontal load caused by the braking forces of the road surface. These vertical loads are applied to the leaf spring face of the front axle, while horizontal loads are applied to the bolt mounting holes of the leaf spring face.

By setting intrinsic constraints within the kingpin bore and implementing vertical loads on the two leaf spring faces, these loads are evenly distributed across the two leaf spring faces of the entire front axle. A lateral load is also set in the ten screw holes on the front axle, which is also evenly distributed to each screw hole. The braking condition of the front axle is shown in Figure 4 as a loading boundary condition.

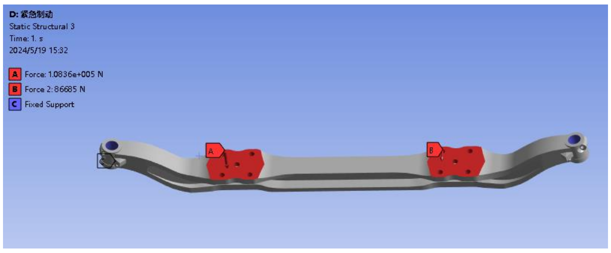

Figure 4 Load boundary conditions for emergency braking conditions

As shown in Fig. 5, when the vehicle is subjected to a sudden braking action, the main deformation of the front axle occurs in the middle part of the vehicle, and the most significant change occurs in the rear side area located at the top of the I-beam. In addition, it is found that the deformation at the top of the front axle is greater than that at the bottom, and the increase in deformation moves from the top to the bottom of the I-beam. Full constraints are set in the kingpin hole of the front axle, so the deformation of this part is relatively small; As you get closer to the kingpin hole, the deformation increases to a maximum of 2.74 mm and is concentrated in the center of the front axle.

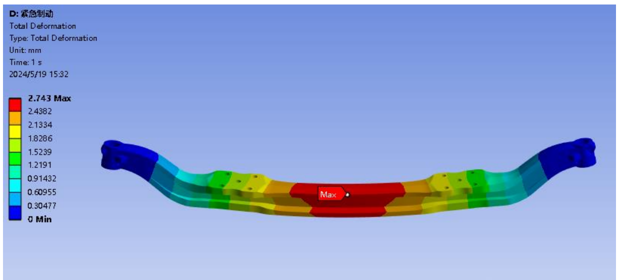

Figure 5 Contour of front axle deformation under emergency braking conditions

As shown in Fig. 6, in the middle of the front axle, the main bending stress of the I-beam is mainly concentrated in the boundary area of the fenders on both sides of it. Because the bolt holes on the leaf spring of the front axle contain the transverse load, the stress of the fender on the front axle is greater than that of the lower fender, and the boundaries of the front and rear sides of the fender on the front axle have significant bending stresses, while the tail end of the lower fender has obvious bending stress, and the bending stress distributed at the web of the I-beam is the smallest. The most serious bending stress on the front axle reaches 355.5 MPa, but this value is far less than the compressive limit of 42CrMo of 930 MPa, so the safety performance of the front axle can be guaranteed in the case of hard braking.

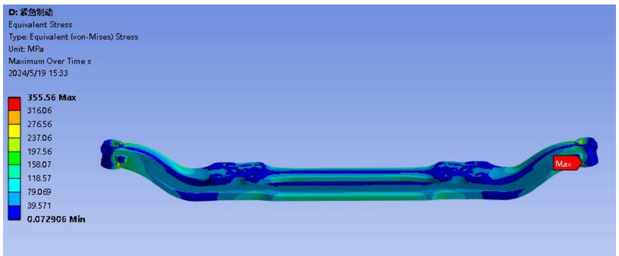

Figure 6 Front axle stress contour under emergency braking conditions

2.2.2 Finite element analysis under uneven pavement conditions

When a car crosses an uneven road, the front axle is mainly subjected to vertical impact loads from road impacts, which act on the leaf spring surface in an evenly distributed manner.As shown in Figure 7, vertical impact loads are applied evenly on the two leaf spring surfaces of the front axle so that these loads are evenly distributed to the two leaf spring faces of the front axle. Full constraints are placed at the kingpin holes of the front axle to prevent its displacement.

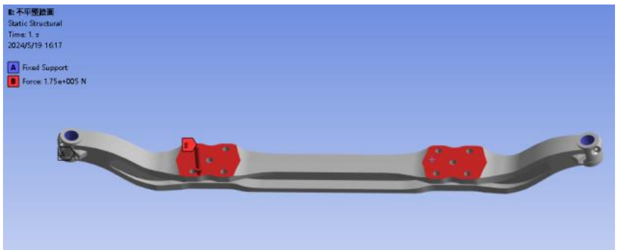

Figure 7 Load boundary conditions for uneven pavement conditions

The stress and deformation of the front axle are obtained through simulation analysis, as shown in Fig. 8 and Fig. 9. Looking at these images, it can be seen that the deformation of the center of the front axle is most pronounced during the bumpy road section, and the degree of deformation exceeds that of the front axle when it is only subjected to the heavy braking load. Compared with the front axle, which independently receives the vertical impact force, this part shows a more balanced deformation state when dealing with the lateral impact force, and on the whole, the deformation of the central area is larger, while the two sides are relatively small, and the most significant deformation occurs in the middle of the front axle, which is about 1.26 mm.When the front axle is subjected to shock loads, the bending stress generated by the upper part of the I-beam in the middle is relatively small, and it is also relatively small on the leaf spring surface of the front axle. The lower wing of the I-beam of the front axle generates large and concentrated bending stresses, especially in the web area, which even exceed the bending stress of the upper wing. The overall bending stress of the front axle reaches a maximum of 201.7 MPa, but this is far less than the stress yield limit of 930 MPa for this material, so the safety performance of the front axle is guaranteed during driving under such non-uniform road conditions.

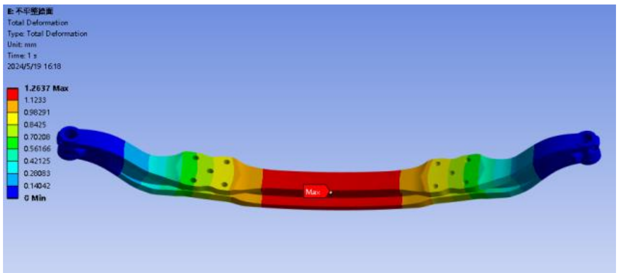

Figure 8 Front axle deformation contour under uneven pavement conditions

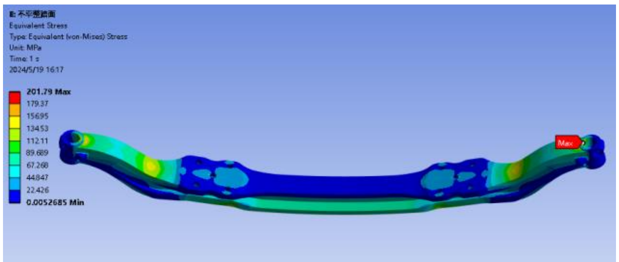

Figure 9 Front axle stress contour under uneven pavement conditions

2.2.3 Finite element analysis in sideslip conditions

When the car slips sideways during rotation, the left and right leaf springs of the front axle produce a change in the vertical load. The lateral forces exerted by the ground on the wheels subject the front bearing to lateral forces, which are stored in the bolt holes of the front axle in an evenly distributed manner.As shown in Figure 10,the vertical load on the front bearing is distributed to the leaf spring surface of the front axle on both sides of it, and the lateral forces due to inertia and acting on the leaf spring surface of the front axle should be taken into account, which should be achieved by distributing it to the bolt holes on the leaf spring surface on both sides of the front axle. Set full constraints in the kingpin hole on the front axle.

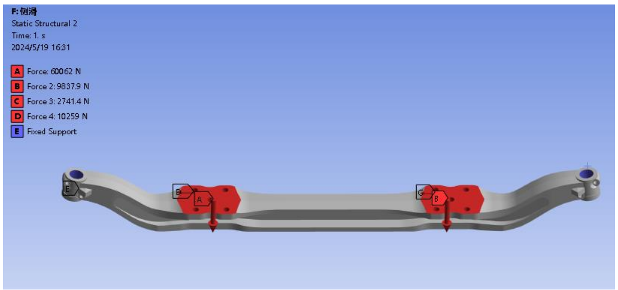

Figure 10 Load boundary conditions for sideslip cases

As shown in Fig. 11, when the vehicle is in a side-slip state, the left and right leaf spring surfaces of the front axle need to bear a new vertical load distribution, which makes the deformation of the front axle show an asymmetrical change, which is more obvious than the equilibrium form in the previous two working conditions. The maximum measure of the bending deformation of the front axle is 0.57 mm, mainly from the leaf spring surface in the left half of the front axle to the middle of the I-beam.

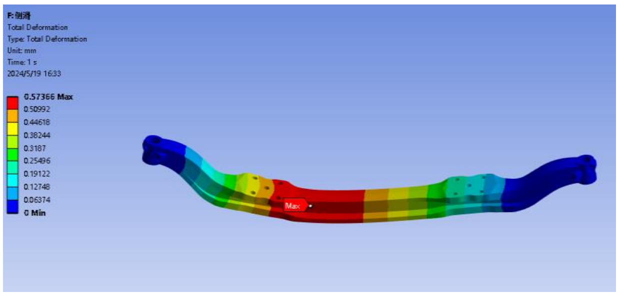

Figure 11 Deformation contour of the front axle under the side-slip condition

As shown in Figure 2, if the vehicle skids, the axle on the left side of the front wheel is subjected to significantly greater bending stress than on the right part of the front axle, and this stress is more concentrated. In this case, the maximum bending stress on the front axle is 199.71 MPa, but this is also much less than the compressive limit of 930 MPa for this material, which occurs in a circular opening area near the bottom of the kingpin hole. Therefore, in the sideslip state, the safety performance of the front wheels is guaranteed.

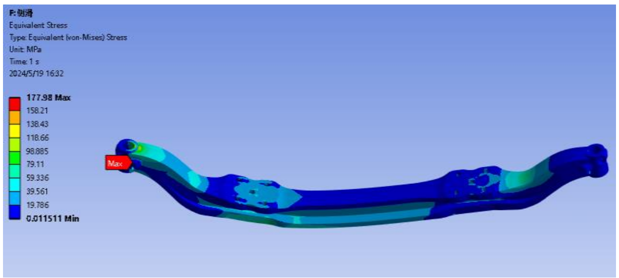

Figure 12 Front axle stress contour under sideslip conditions

Table 2 Maximum stress and maximum deformation for three operating conditions

Operating conditions	Maximum stress/ MPa	Maximum deformation/ mm
Emergency braking	355.5	2.74
Uneven pavement	201.7	1.26
Sideslip	199.71	0.57

As shown in Table 2, the maximum stress and maximum deformation of the three typical working conditions, the maximum stress is less than the compressive limit of 42CrMo material 930MPa, which meets the requirements, and the data in the table can also understand that under the emergency braking condition, the stress and deformation are the largest, so in order to ensure the safety of the structure, the topology can be optimized for the load of the emergency braking condition.

3 Lightweight Design of the Front Axle of The Car

3.1 Lightweight design of the front axle

After completing the stiffness evaluation of the front wheel in three working states, it was found that it bears the maximum stress under emergency braking. Therefore, the simulation results of front axle deformation and stress under emergency braking conditions were input into the ANSYS Workbench structural optimization tool. The optimization goal was set to retain 60% of the front axle mass. The restricted and optimized areas are shown in Figure 13, and the optimization parameter settings are shown in Figure 14.

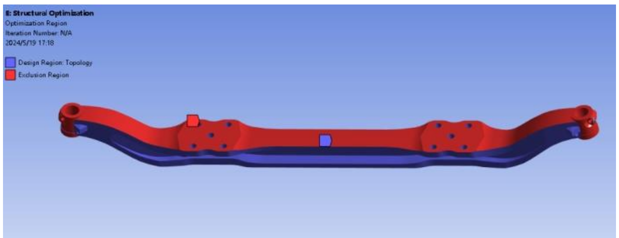

Figure 13 Optimize regional constraints

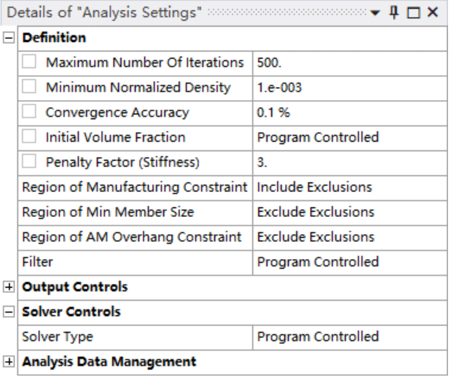
Details of "Analysis Settings"

Definition	
☐ Maximum Number Of Iterations	500.
☐ Minimum Normalized Density	1.e-003
☐ Convergence Accuracy	0.1 %
☐ Initial Volume Fraction	Program Controlled
☐ Penalty Factor (Stiffness)	3.
Region of Manufacturing Constraint	Include Exclusions
Region of Min Member Size	Exclude Exclusions
Region of AM Overhang Constraint	Exclude Exclusions
Filter	Program Controlled
Output Controls	
Solver Controls	
Solver Type	Program Controlled
Analysis Data Management	

Figure 14 Optimize parameter settings

As shown in Figure 15, when the vehicle is in an emergency braking state, the topology optimization of the front axle focuses on the web plate of the I-shaped crossbeam in its central part, and the optimization adjustment of the front wheel structure is completed by drilling three holes. Based on the strength assessment under emergency braking conditions, the grid constructed is used as the basis. The optimization calculation of ANSYS Workbench produces the results of the front axle, which is an ideal state and can provide guidance for the design and optimization of the front wheel model. However, the specific optimization strategy must take into account the manufacturing costs and costs in reality. Based on the optimization results, the front axle model is modified on SolidWorks, and the optimized model is shown in Figure 16. By comparing the quality of the model before and after optimization, a total weight reduction of 6.73% was achieved in this structural optimization.

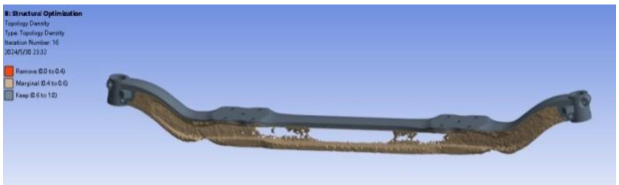

Figure 15 Front axle topology optimization results under emergency braking conditions

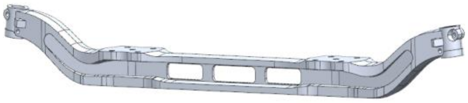

Figure 16 Optimized 3D model

3.2 Static analysis of the optimized front axle

3.2.1 *Finite element analysis under emergency braking conditions*

As shown in Figures 17 and 18, it can be seen that the main bending deformation of the front axle occurs in its middle part, while the part around the main pin hole is relatively stable. As it gets closer to the main pin hole, the degree of deformation gradually increases to a maximum value of 2.76mm, which mainly occurs in the central area of the front axle.In the middle of the front axle, the bending stress borne by the I-beam is mainly distributed at the edges of the upper and lower fenders. The maximum bending stress value reaches 380 8MPa, which is much lower than the yield strength of the material, makes the front axle safe in emergency braking conditions.

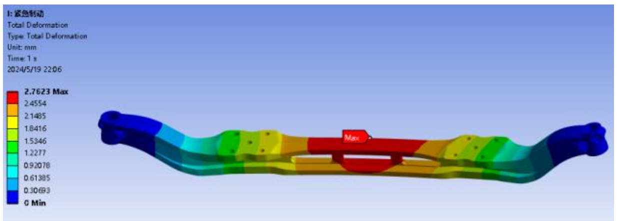

Figure 17 Cloud map of front axle deformation under emergency braking conditions

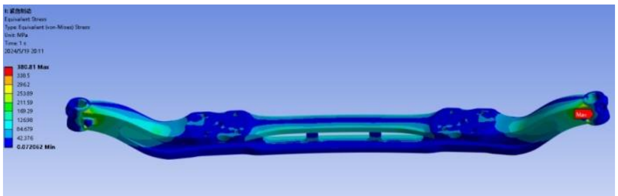

Figure 18 Front axle stress cloud map under emergency braking conditions

3.2.2 *Finite element analysis under uneven road conditions*

As shown in Figures 19 and 20, it can be observed from the images that during the process of vehicles crossing uneven roads, the deformation degree of the middle part of the front axle is the most significant, with a larger deformation in the central area and smaller deformation on both sides as a whole. The deformation of the upper and lower ends of the front axle is roughly the same, and the deformation of the entire front axle is very regular.

The most obvious deformation is located in the middle of the front axle, with a size of approximately 1.28mm. Under the impact load, the peak bending stress of the front axle reaches 204 1MPa mainly occurs on the cross-section at the connection between the main pin hole and the circular arc segment. This value is much lower than the yield strength of the material of 930MPa. Therefore, even in uneven road conditions, the front axle is still safe.

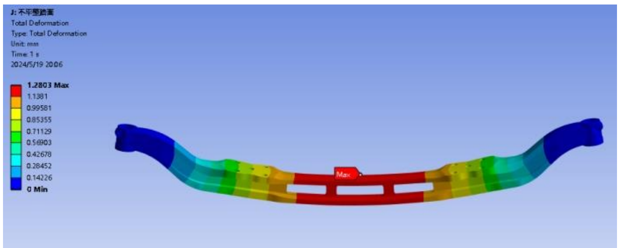

Figure 19 Cloud map of front axle deformation under uneven road conditions

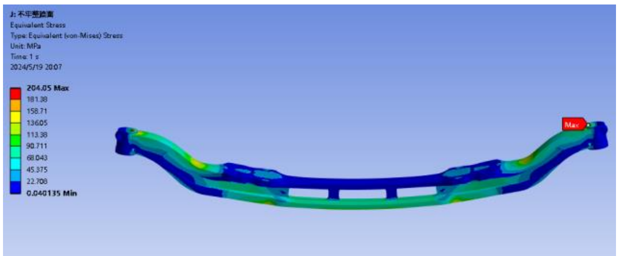

Figure 20 Front axle stress cloud map under uneven road conditions

3.2.3 *Finite element analysis under lateral sliding conditions*

The simulation analysis shows the stress and deformation status of the front wheel, as shown in Figures 21 and 22. Observing the images, it can be seen that when the vehicle slides to the right during rotation, the maximum bending deformation of the front axle reaches 0.72mm, mainly concentrated in the area from the leaf spring surface on the left side of the front axle to the front crossbeam in the middle.

In the case of a car rotating and experiencing sideslip, the distribution of bending stress on the axle is generally similar to the distribution of bending deformation on the front axle. In this case, the maximum bending stress reached 210.9 MPa, which is much lower than the compressive limit value of 930 MPa for this material. This stress is mainly concentrated in the circular area below the main pin hole and at the edge of the front axle. So, in this situation, the front wheel safety performance is good.

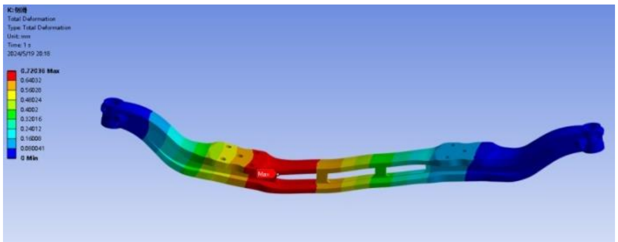

Figure 20 Cloud map of front axle deformation under sideslip condition

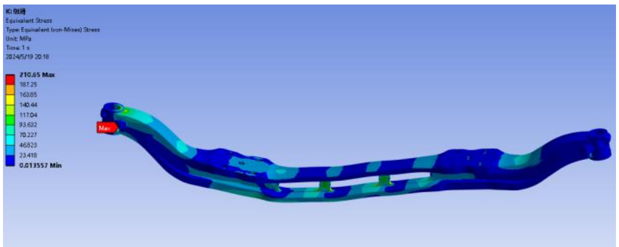

Figure 21 Front axle stress cloud map under sideslip condition

3.2.4 Analysis of stress-strain situations under various working conditions

As shown in Table 3, the maximum stress and deformation of the optimized front axle under three typical working conditions are shown. The maximum stress is 380.8 MPa under emergency braking, which is less than the compressive limit of 930 MPa of 42CrMo material. This meets the requirements and verifies the feasibility of the optimized model.

Table 3 Maximum stress and maximum deformation under three working conditions

Operating conditions	Maximum stress/ MPa	Maximum deformation/ mm
Emergency braking	380. 8	2.76
Uneven pavement	204. 1	1.28
Sideslip	210.9	0.72

4 Fatigue Life Analysis of Automotive Front Axles

Usually, fatigue life research is based on the results of finite element simulation, extracting stress or deformation stress charts from key parts of the structure, then statistically analyzing these charts, and finally evaluating the life based on the fatigue characteristics and damage principles of the structural material. Figure 22 shows the S-N curve of 42CrMo material in ANSYS.

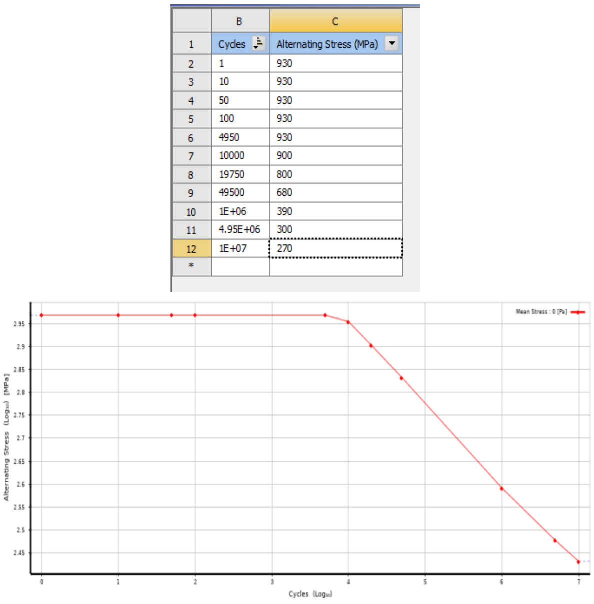

	B	C
1	Cycles	Alternating Stress (MPa)
2	1	930
3	10	930
4	50	930
5	100	930
6	4950	930
7	10000	900
8	19750	800
9	49500	680
10	1E+06	390
11	4.95E+06	300
12	1E+07	270
*		

Figure 22 S-N curve of 42CrMo material in ANSYS

According to the results of strength finite element analysis under three different working conditions before and after optimizing the weight of the front axle, it was found that the weight optimization of the front axle resulted in the maximum factor under emergency braking conditions. Therefore, the Fatigue Tool module of ANSYS Workbench was used to conduct fatigue analysis on the front axle under emergency braking conditions. The parameter settings of the analysis interface are shown in Figure 23.

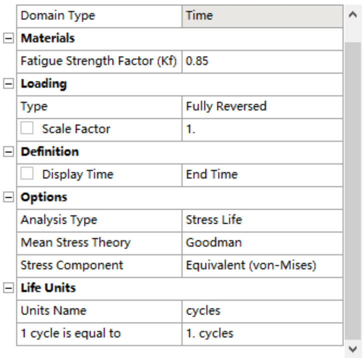

Domain Type	Time
Materials	
Fatigue Strength Factor (Kf)	0.85
Loading	
Type	Fully Reversed
☐ Scale Factor	1.
Definition	
☐ Display Time	End Time
Options	
Analysis Type	Stress Life
Mean Stress Theory	Goodman
Stress Component	Equivalent (von-Mises)
Life Units	
Units Name	cycles
1 cycle is equal to	1. cycles

Figure 23 Fatigue Tool Analysis Interface Settings

According to the fatigue life assessment results shown in Figure 5.5, it was found that the maximum stress point corresponds to the lowest fatigue life. The optimized value is approximately 4.72 x 105 cycles, which is greater than low cycle fatigue by 1 x 105 and is within a reasonable range.

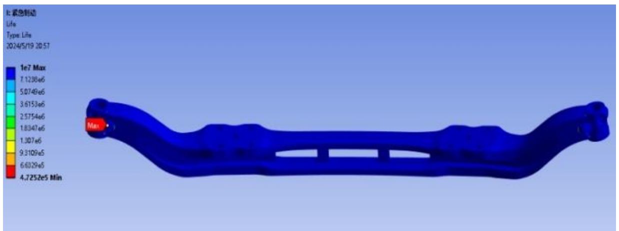

Figure 24 Cloud map of fatigue life analysis after front axle optimization

5 Conclusion

This article takes the TR01 front axle as the main object and creates its finite element model. A thorough exploration and finite element analysis were conducted on the possible loads and their application methods that the front axle may face under three typical working conditions: emergency braking, sideslip, and uneven road conditions, in order to obtain the stress and deformation values generated by the front axle under these conditions. The following conclusions can be drawn:

(1) In emergency braking and vehicle crossing rough roads, the load and direction of force borne by the front wheels are relatively balanced, so the stress and deformation simulation data on both sides also show consistent distribution characteristics. When the vehicle deviates from its trajectory, the main part of the stress and deformation simulation data of the front wheel will appear on the left spring I-beam, and the stress of the front wheel in these three cases is far lower than the yield strength value of the material.

(2) Optimization design of the front axle.Given that the topology optimization of the front axle under emergency braking mainly occurs in the web area of the middle I-beam, in this case, the topology optimization strategy of the front axle is to excavate three holes at the middle web position.

(3) To evaluate whether the minimum fatigue life of the optimized front axle meets the requirements, the finite element modeling of the optimized front axle parts can be re imported into the static analysis module to calculate the stress levels under three working states. It was found that the stress generated by the optimized front axle under these three conditions is significantly lower than the yield stress value of its material; And compared it. After optimizing the fatigue life of the front axle, the simulation results show that the minimum fatigue life of the optimized front axle meets the requirements.

Reference

[1] Lee Y L, Pan J, Hathaway R, etal．Fatigue Testing and Analysis [M]. New York: Elsevier Inc, 2005.

[2] Allegri G,Zhang X．On The Inverse Power Laws for Accelerated Random Fatigue Testing [J]. International Journal of Fatigue, 2008(30):967-977．

[3] Benasciutti D,TovoR．Frequency Based Analysis of Random Fatigue Loads: Models, reality [J]. Material Wissen Schaft and Werk Stoffte Chnik, 2018,3(49):345-367．

[4] Han Q,J Li, J Xu, etal.A New Frequency Domain Method for Random Fatigue Life Estimation in a Wide-band Stationary Gaussian Random Process [J]. Fatigue & Fracture of Engineering Materials & Structures, 2018,42(10-11).

[5] Yuan Y H ,He W M .Based on 3D Virtual Prototype Technology and Finite Element Analysis of the Optimization of the Automobile Front Axle [J]. Applied Mechanics and Materials, 2014,3615(684-684):330-334.

Publisher: Viser Technology Pte. Ltd.

URL: www.viserdata.com

Add.:111 North Bridge Rd, #21-01 Peninsula Plaza,

Singapore 179098

ISSN 2661-443X

9 772661 443250 01